FREQUENCY REDUCTION AND ATTENUATION OF THE TIRE AIR CAVITY MODE DUE TO A POROUS LINING

by

Kyosung Choo

A Thesis

Submitted to the Faculty of Purdue University

In Partial Fulfillment of the Requirements for the degree of

Master of Science in Mechanical Engineering

School of Mechanical Engineering

West Lafayette, Indiana

May 2023

THE PURDUE UNIVERSITY GRADUATE SCHOOL
STATEMENT OF COMMITTEE APPROVAL

Dr. John Stuart Bolton, Chair
School of Mechanical Engineering

Dr. James Gibert
School of Mechanical Engineering

Dr. Vikas Tomar
School of Aeronautics and Astronautics

Approved by:
Dr. Nicole L. Key

Fall Forward.

ACKNOWLEDGMENTS

I would like to express my gratitude to the following individuals who have supported and encouraged me throughout my academic journey and the completion of this thesis.

First and foremost, I would like to thank my thesis advisor, Dr. J. Stuart Bolton, for his guidance, encouragement, and patience throughout this project. His expertise and insights have been invaluable in shaping this research. I would also like to thank my committee members, Dr. James Gibert and Dr. Vikas Tomar, for their time and effort in reviewing my work and providing valuable feedback.

My heartfelt thanks go to my wife, Yujeong, and my kids, Sion and Yeon, for their unwavering support, encouragement, and understanding throughout my academic journey. Their love and sacrifices have been my source of strength and motivation.

Finally, I would like to thank Won Hong Choi, Guochenhao Song, and Zhuang Mo for generously volunteering their time and insights for this study. Their contributions have been essential to the success of this project, and I am grateful for their participation.

Thank you all for your support and encouragement.

TABLE OF CONTENTS

LIST OF TABLES

LIST OF FIGURES

NOMENCLATURE

$\tilde{k}_c$	Complex wavenumber of a porous material
$\tilde{z}_c$	Specific characteristic impedance of a porous material
$\tilde{z}_n$	Specific normal surface acoustic impedance
c_o	Sound speed of air
$\tilde{c}$	Complex sound speed within porous material
ω	Angular frequency
f	Temporal frequency
σ	Flow resistivity
ϕ	Porosity
α_∞	Tortuosity
Λ	Viscous characteristic length
Λ'	Thermal characteristic length
$\tilde{\rho}$	Complex density of a porous material
$\tilde{B}$	Complex bulk modulus of a porous material
ρ_o	Air density
η	Air kinematic viscosity
γ	Fluid specific heat ratio
κ	Thermal conductivity
p_o	Acoustic pressure in airway
$\tilde{p}$	Acoustic pressure within porous material
k	Wavenumber in airway
k_x	Axial component of wavenumber in airway
k_y	Transverse component of wavenumber in airway
$\tilde{k}$	Wavenumber in porous layer
$\tilde{k}_x$	Axial component of wavenumber in porous layer
$\tilde{k}_y$	Transverse component of wavenumber in porous layer
u_o	Normal particle velocity in airway
$\tilde{u}$	Normal particle velocity in porous layer
L_c	Axial length of a duct model (= average circumferential length of a tire)
h_a	Height of airway in a duct model
h_t	Height of duct in a duct model
t_p	Thickness of porous layer

ABSTRACT

The tire air cavity mode is known to be a significant source of vehicle structure-borne road noise near 200 Hz. A porous lining placed on the inner surface of a tire is an effective countermeasure to attenuate that resonance. The two noticeable effects of such a lining are the reduction in frequency and the attenuation of the air cavity mode. In this thesis, through both theoretical and numerical analysis, the mechanism of the effects of a porous lining was studied. A two-dimensional duct-shaped theoretical model and a torus-shaped numerical model were built to investigate the lined tire in conjunction with the Johnson-Champoux-Allard model describing the viscous and thermal dissipative effects of the porous material. Design parameters of the porous lining were varied to study their impact and optimal ranges of the design parameters were identified. Finally, in an experimental analysis, the sound attenuation and the frequency drop were observed in measurements of force, acceleration, and sound pressure. In conclusion, it was demonstrated that the suggested theoretical and numerical models successfully predict the effects of porous linings and that the frequency reduction results from the decreased sound speed within the tire owing to the presence of the liner.

1. INTRODUCTION

1.1 Background of Study

The NVH (noise, vibration, and harshness) challenges presented by electric vehicles in the automotive industry are unique. The absence of a traditional powertrain causes interior structure-borne road noise to become more audible and prominent due to the disappearance of the masking effect provided by the internal combustion engine noise. As a result, at low speeds, road noise becomes the primary source of disturbance for passengers, as depicted in Figure 1.1.

One significant contributor to the structure-borne road noise is the vibration originating from the Tire Air Cavity Resonance (TACR). When a tire is rolling on a macro-rough surface, not only the tire structure but also the air cavity inside the tire is excited. The air trapped in the tire has its natural modes, with its first natural mode called the cavity mode, as shown in Figure 1.2. This cavity mode lies around 200 Hz for currently typical passenger car tires, and the frequency varies depending on the tire's size. The tire air cavity resonance creates acoustic pressure that excites the wheel, and the resulting vibration of the wheel due to the TACR is transmitted to the suspension, body, and ultimately reaches the vehicle cabin. This type of structure-borne noise transmission is depicted in Figure 1.3.

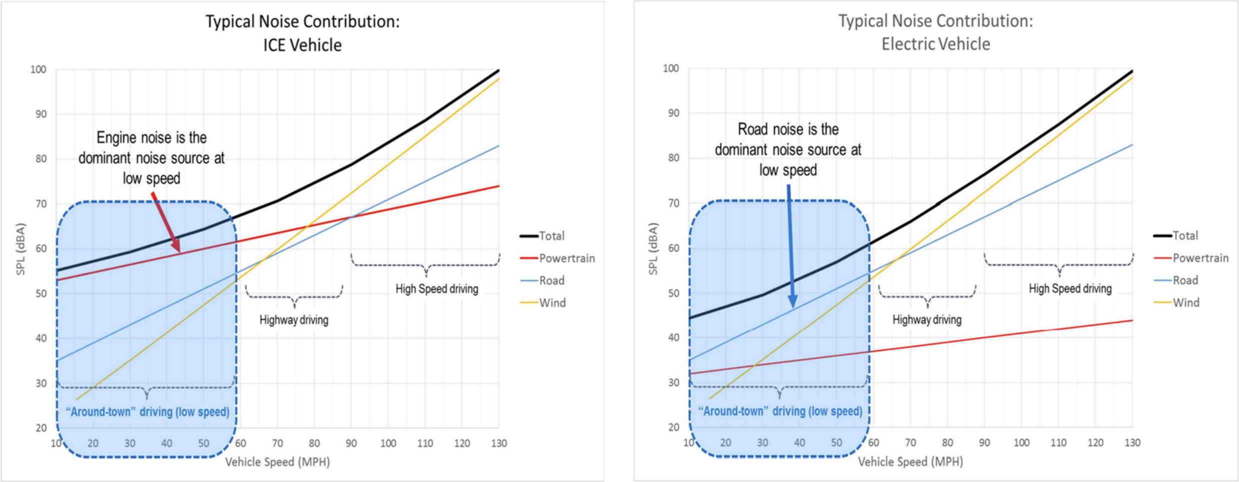

(a) Typical Noise Contribution of ICE vehicle

(b) Typical Noise Contribution of Electric Vehicle

Figure 1.1. Comparison of noise contribution between internal combustion engine vehicles and electric vehicles [1].

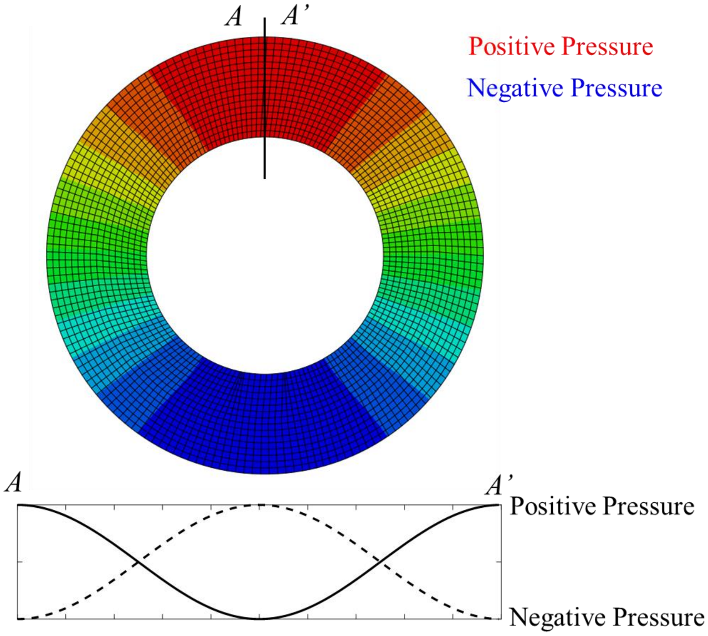

Figure 1.2. Pressure distribution in the first air cavity resonance of a tire.

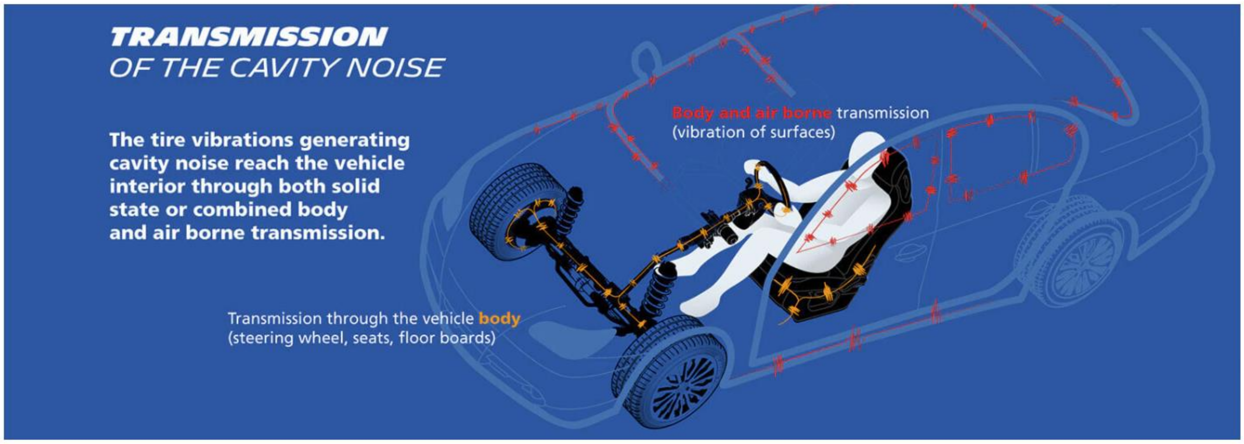

Figure 1.3. Transmission of structure-borne tire air cavity noise [2].

The TACR noise is particularly troublesome since it produces a peak in a narrow frequency range with a relatively high amplitude, which is easily detectable by the human ear. Figure 1.4 shows the interior noise measurements of two different vehicles and tires. Although the level of the TACR noise is different depending on the vehicle and tire, the noise is prominent in both cases over the frequency range up to 800 Hz.

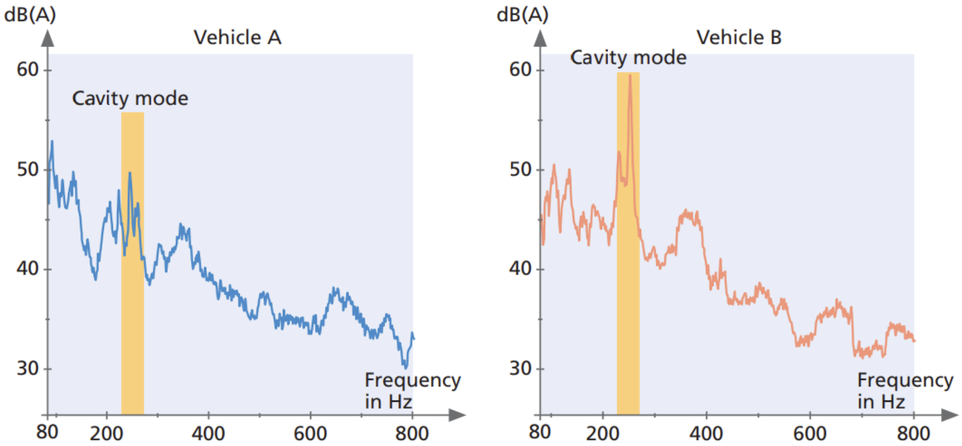

Figure 1.4. Frequency spectrum of road noise and tire air cavity resonance mode [3].

To review some of the previous articles that serve as milestones in TACR research, Sakata et al. [4] were the first to discuss the noise issue. They related the peak noise in the cabin to the tire cavity resonance by comparing the sound pressure levels at the driver's ear position with the hub vertical acceleration during an on-road coasting test. They demonstrated that the vibration and tire noise are mainly influenced by the first mode of the cavity resonance. Figure 1.5 shows the modes of the tire cavity resonance, including its harmonics, which are multiples of the fundamental resonance. One key observation is that only the first mode of the cavity resonance creates a net force that vertically excites a wheel, while the higher modes do not create a net force. Since Sakata's initial research, several studies have been performed to analyze the influence of tire deflection in the contact patch area by Thompson [5,6], rolling speed by Feng et al. [7-11], and the coupling mechanisms between the air cavity and the rim/tire structure by Cao and Bolton [12,13].

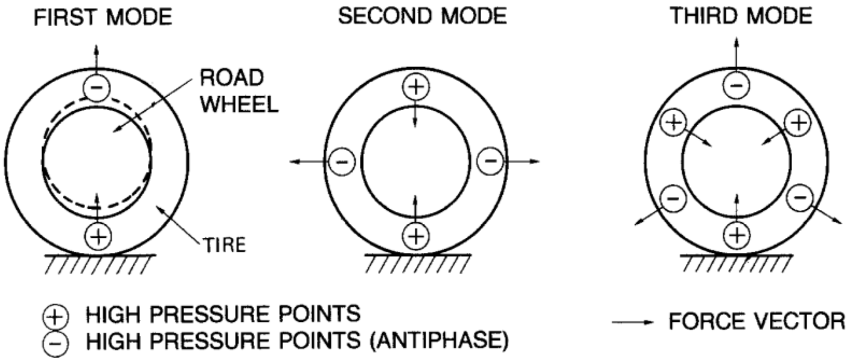

Figure 1.5. The first, second, and third modes of tire air cavity resonance [4].

1.2 Literature Review of Porous Lined Tire

Various solutions have been proposed to address tire cavity resonance noise, but only a few have been successfully commercialized due to various constraints and challenges. Of the mass-produced solutions, the porous lining of a tire is an effective and widely adopted countermeasure that has received significant attention in recent years. Several theoretical and numerical models that incorporate porous material propagation models have been proposed to simulate the noise attenuation effects.

For instance, Baro et al. [14] developed a numerical model of the tire cavity with porous lining and analyzed the frequency response functions (FRF) for a fixed set of material properties. In their research paper, they proposed a 3-dimensional finite element (FE) model to predict the damping performance of a lined tire. The authors evaluated the damping performance by comparing the point acoustic impedance at the center of the excitation patch for the non-lined tire and lined tire FE models. Figure 1.6 displays the finite element model with porous lining and the frequency response of the simulation. Their research revealed that, for fixed material characteristics, the volume of the lining treatment had a strong influence on the cavity resonance.

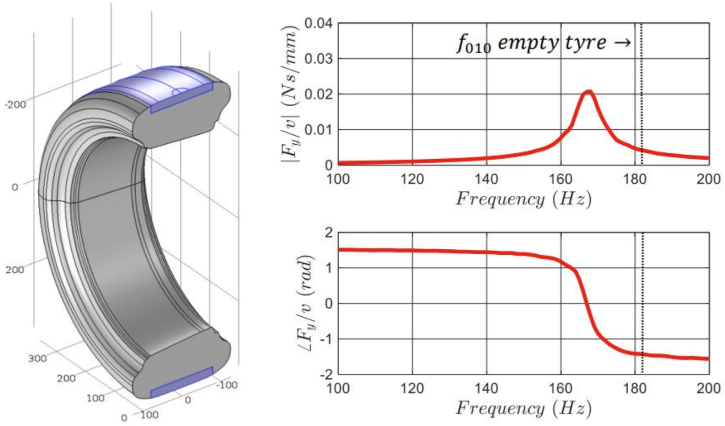

Figure 1.6. FE model and FRF result of the air cavity of 20 inch tire lined with polyurethane foam [14].

In their second paper [15], Baro et al. further studied the design optimization of the porous layer in terms of its geometric layout. Figure 1.7 shows the design cases they simulated to compare their effectiveness in attenuation. One key finding was that the attenuation of the cavity resonance could be increased without changing the volume of sound-absorbing material by selecting a discontinuous layout. In Figure 1.8, the point acoustic impedance of the non-lined and lined cases are compared. The point acoustic impedance of design case (d), which features the discontinuous layout, is lower than that of design case (b), which has a normal continuous layout, while the volumes of (b) and (d) are the same. The discontinuous layout is a good idea, but the reason for its better attenuation was not explained in detail. Additionally, their research was limited to a case in which the porous material properties were fixed.

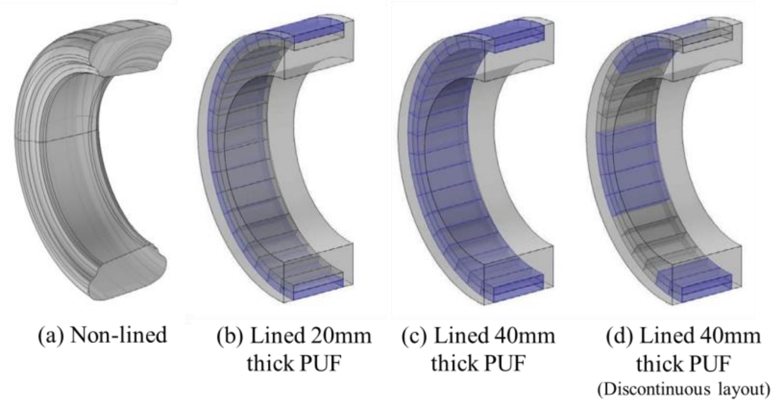

Figure 1.7. FE models of tire cavity of non-lined and lined tires [15].

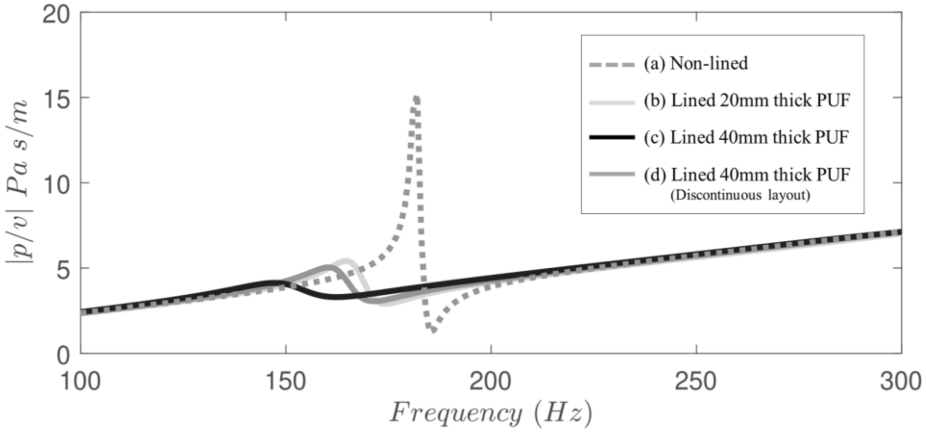

Figure 1.8. Comparison of the point acoustic impedance evaluated at the center of the excitation patch for the FE models [15].

Regarding the investigation of porous material properties, Zhang et al. [16, 17] proposed an eigenvalue analysis of a lined tire in cylindrical coordinates, as depicted in Figure 1.9. By using an equivalent fluid model to represent the sound-absorbing material, the resonance of a lined tire cavity can be transformed into a complex eigenvalue problem. The Delany-Bazely-Miki (DBM) model was used to describe the acoustic characteristics of the sound-absorbing material, with flow resistivity being the single parameter of the DBM model. Based on the eigenvalue analysis, the complex frequency was plotted as a function of flow resistivity.

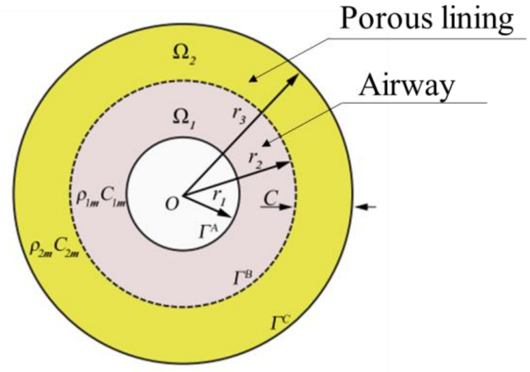

Figure 1.9. Schematic diagram of the tire cavity lined with the porous material [17].

Building on the research of Zhang et al. [16], Wan et al. [17] used a multi-domain boundary element method (MBEM) to assess the impact of porous materials on controlling tire cavity resonance and proposed optimal parameters for the porous material. The DBM model was selected to describe the sound propagation model in the porous material. The simulation yielded successful results, which were validated experimentally. Figure 1.10 illustrates the simulation results, demonstrating the effect of changing design parameters, specifically flow resistivity. The primary finding of this research, as shown in Figure 1.11, was the introduction of the shifting procedure of the real and imaginary part of the cavity frequency with the change of flow resistivity of the porous material for different thicknesses and widths. The imaginary part of the cavity frequency represents the damping loss resulting from the porous material. The authors found that a flow resistivity around 1,850 N s⁄m4 or Rayls/m was optimal, and thicker or wider porous material provides better attenuation for cavity resonance noise. The proposed method is an effective tool for selecting the flow resistivity, thickness, and width of the porous material.

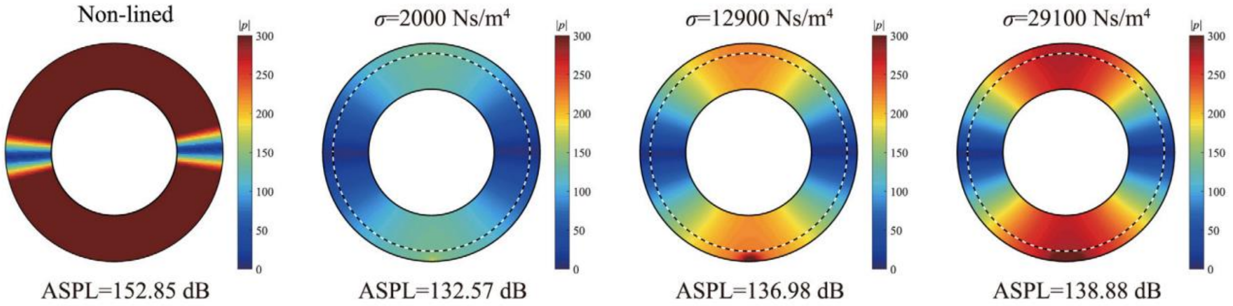

Figure 1.10. The pressure field of the cross-section diagram of the tire cavity non-lined/lined with the porous material of different flow resistivities [17].

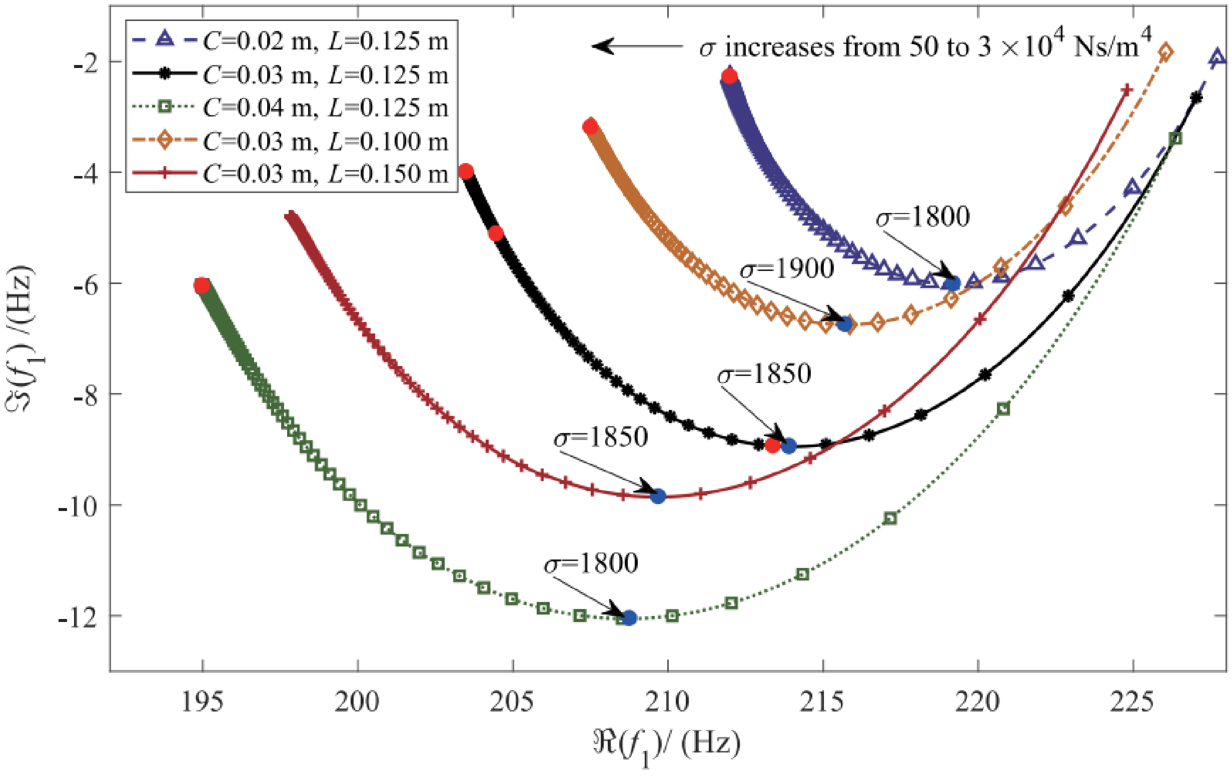

Figure 1.11. The shifting procedure of the first eigenfrequency f_1 with the change of the porous material flow resistivity, when different thickness, *C*, and widths, *L*, are considered [17].

1.3 Research Objective

Previous studies were commonly based on the assumption that sound propagation in porous materials could be accurately modeled using the Delany-Bazely-Miki model (DBM model) [18,19]. In general, that one-parameter empirical model is suitable for high porosity, porous linings. However, due to its empirical nature, the design parameters in that model are constrained to lie within the boundaries shown in Figure 1.12.

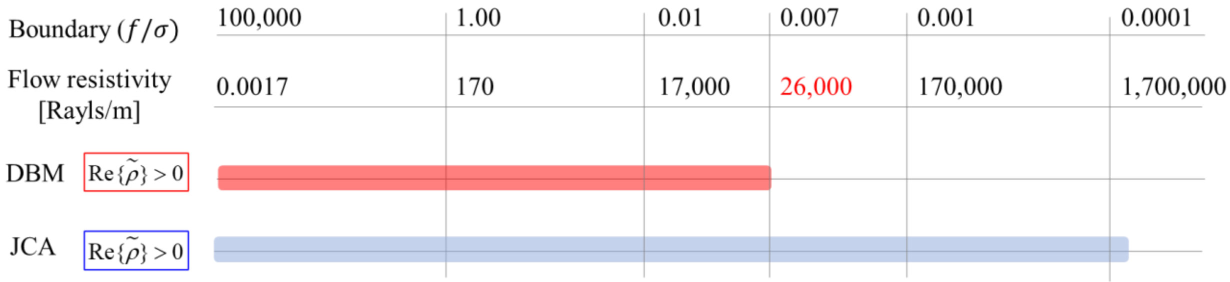

Figure 1.12. Working boundary of the flow resistivity in DBM and JCA model

The focus of the current study was to investigate broader design parameter boundaries by employing a more advanced propagation model, the Johnson-Champoux-Allard model (JCA model) [20,21], and also to identify the sound attenuation and frequency reduction mechanisms. Furthermore, the implementation of the five-parameter semi-phenomenological model, the JCA model has resulted in the identification of an additional optimal design range compared to previous studies.

In addition, the other objectives of this research were to develop a systematic and comprehensive methodology to analyze and predict the effect of porous linings on the tire air cavity resonance. Specifically, the goals here were to identify the mechanisms of sound attenuation and frequency reduction of the tire air cavity resonance (TACR), to visualize the effect of sound attenuation and frequency reduction of the TACR, to predict and validate the sound pressure and force mitigation of the TACR under various boundary conditions, and to suggest optimal design parameters of the porous material.

2. PROPAGATION MODELS OF POROUS MATERIALS AND ACOUSTIC MODEL OF A LINED TIRE

2.1 Introduction

Porous materials are effective sound-absorbers because they convert acoustical energy into heat. The primary mechanism for sound absorption by porous materials is achieved by the visco-inertial and thermal dissipative effects of the material. By considering these effects, the propagation of sound in porous materials can be modeled to compute their acoustical properties.

This chapter will begin with an explanation of the mechanisms of visco-inertial and thermal dissipative effect of porous material. Next, two sound propagation models of porous materials, namely the DBM model and the JCA model will be compared. The decision to use the JCA model will be explained as well. In addition, an acoustic model of a lined tire will be proposed, and by implementing appropriate boundary conditions, and as an outcome of the model, a transcendental equation will be derived from the model. Finally, this chapter will include a discussion of how the sound propagation model of a porous material and the acoustic model of a lined tire will be integrated to compute the axial wavenumber in the tire air cavity. The behavior of the axial wavenumber will be further discussed with respect to the change in design parameters of porous materials.

2.2 Dissipative Effects of Porous Materials

The use of a porous material lined tire can reduce tire air cavity resonance because acoustical energy inside the tire is dissipated as it interacts with the porous materials. To fully understand this mechanism, it is crucial to have a thorough understanding of porous materials. Porous materials are composed of two phases: the solid, typically fibrous component known as the frame, and the fluid that fills the pores formed by the frame, typically air [22]. Figure 2.1 depicts the magnified view of a porous material, polyurethane acoustic foam, and a schematic of the solid and fluid components of the material. The dissipation of acoustical energy in porous materials is primarily achieved through the interaction of the solid and fluid phases. The interaction of the solid and fluid phases occurs through various mechanisms, such as viscous means that involve the shearing of the fluid in the boundary layer formed on the fibrous surface and thermal means that represents irreversible heat transfer between fluid and solid [22].

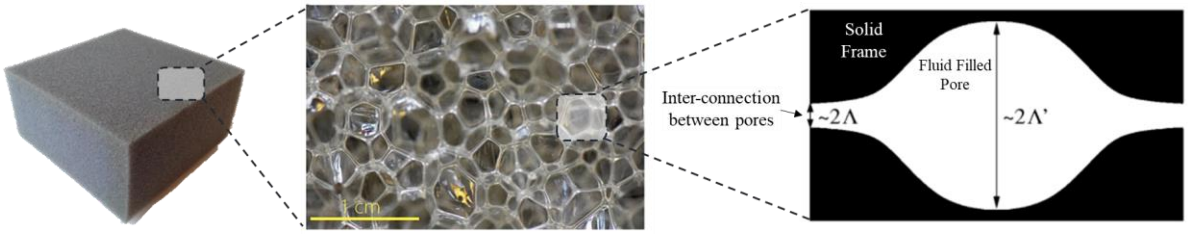

Figure 2.1. Magnified view of polyurethane acoustic foam and schematic of its solid and fluid components [23-25].

To be more specific about each effect, the viscous-inertial effect can be divided into two parts: the viscous effect and the inertial effect. First, the viscous effect is defined as the dissipation of acoustical energy in the form of heat due to internal friction in the boundary layers. The boundary layer formed on the solid walls, including pores and inter-connections, produces a gradient in particle velocity as shown in Figure 2.2. The velocity difference between the layers creates shearing of the fluid, and the resulting internal friction dissipates energy in the form of heat. Next, the inertial effect also plays an important role in energy dissipation, which is concentrated at the inter-connections of pores. The small radius of the inter-connections creates resistance to acoustic flow propagation. This resistance also works as an internal friction, dissipating acoustical energy. Based on the mechanisms explained above, a design parameter of porous material, called the viscous characteristic length (VCL), Λ, is defined as the value of the radius (or hydraulic radius) of the inter-connections depicted in Figure 2.1, and this value usually ranges from 10 to 350 micrometers for typical acoustical materials. [24]

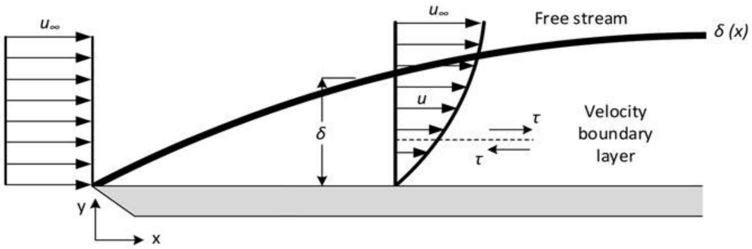

Figure 2.2. Velocity boundary layer on a semi-infinite flat plate [26].

While the visco-inertial effect generates heat, the thermal effect can be considered more of a heat transfer effect. The thermal dissipative effect can be defined as an irreversible heat transfer between the fluid (air) and solid (fibrous component). The heat transfer occurs when a longitudinal sound wave compresses and expands air during the propagation process. During compression of the sound wave, the air heats up, and the heat is transferred to the surrounding solid. During the expansion of the sound wave, the air cools down and pulls back heat energy from the solid. Due to the temperature difference between the fluid and solid, the heat transfer is irreversible. Since the heat transfer mainly occurs in the pores, a relevant design parameter of the porous material is called the thermal characteristic length (TCL), Λ'. This value is close to the radius of the pore, as depicted in Figure 2.1.

2.3 Propagation Models of Porous Materials

The models that describe the propagation of sound in acoustical porous media can be classified into two categories, motionless skeleton model and diphasic model [24,25]. These models differ in their assumptions about the fibrous component and where wave propagation occurs. The motionless skeleton model is based on the assumptions of a rigid frame and that wave propagation occurs only in the fluid that fills the pores formed by the frame. The Delany-Bazely-Miki [18,19] model and the Johnson-Champoux-Allard model [20,21] are examples of this type of model, based on empirical or phenomenological observations. In the diphasic model, the inter-connected fibrous component is assumed to be elastic, and sound waves are considered to propagate in both the fluid and elastic phases. These models integrate Biot theory for elastic wave propagation and a fluid model from the motionless skeleton model, known as the "Biot-JCAL model" [27,28]. The main features of the two model types are summarized in Table 2.1.

In this study, the motionless skeleton model will be used to describe sound propagation in a porous material, despite the fact that the diphasic model offers a more comprehensive description of the vibro-acoustics of porous media. This decision is based on the fact that the motionless skeleton model requires fewer parameters, and both models produce similar results in the frequency range of our interest, below 1 kHz, as depicted in Figure 2.3.

Table 2.1. Classification of the models describing the propagation of sound in porous media.

	Motionless skeleton	Diphasic
Wave propagation	In fluid phase	In both fluid and solid phase
Types of waves	One type (Compression)	Three types (Two compression one transverse)
Material skeleton	Rigid Frame	Elastic frame
Propagation models	Empirical and phenomenological models	Comprehensive models
	Equivalent Fluid model e.g. Delany-Bazely-Miki, Johnson-Champoux-Allard	Biot theory + Fluid model

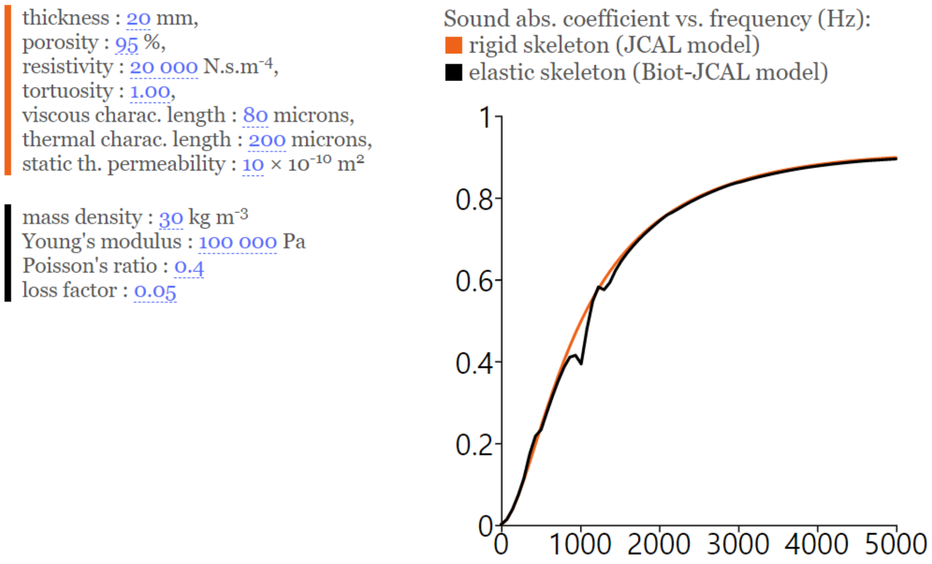

Figure 2.3. Comparison of absorption coefficient between JCAL and Biot-JCAL propagation models [23].

2.3.1 Delany-Bazely-Miki model

Delany and Bazley [18] conducted numerous measurements on fibrous materials with high porosities and developed an empirical formula to represent the complex wavenumber, $\tilde{k}_p$, and specific characteristic impedance, $\tilde{z}_c$, for these materials. Due to its simplicity, their model is still widely used and requires only one parameter, flow resistivity, σ, to describe the acoustic behavior of a material within a certain frequency range. Flow resistivity can be defined as resistance to steady state flow through a porous material [22]. Based on that information, the acoustical performance of porous material can be predicted. Miki [19] further refined this model by proposing modifications to address the non-physical surface impedance behavior in the case of shallow layers. The result was the Delany-Bazley-Miki model, which provides the following expressions for the complex wavenumber, $\tilde{k}_p$, and specific characteristic impedance, $\tilde{z}_c$: i.e.,

$$\tilde{k}_p = \frac{\omega}{c_o}\left[1 + 0.109\left(\frac{f}{\sigma}\right)^{-0.618} - j0.16\left(\frac{f}{\sigma}\right)^{-0.618}\right] \tag{1}$$

$$\tilde{z}_c = \left[1 + 0.07\left(\frac{f}{\sigma}\right)^{-0.632} - j0.107\left(\frac{f}{\sigma}\right)^{-0.632}\right] \tag{2}$$

where c_o is the sound speed, ω represents the angular frequency, and f denotes the temporal frequency. As mentioned in Section 1.3, despite the wide usage owing to its simplicity, the design parameter in this model, the flow resistivity, is constrained to lie within the boundaries shown in Figure 1.12 due to its empirical nature.

2.3.2 Johnson-Champoux-Allard model

In this research, the Johnson-Champoux-Allard model (JCA model) [20,21] was used to describe the propagation of sound in porous materials, as an alternative to the DBM model. The semi-phenomenological JCA model is based on the assumption of non-uniform pore cross-sections and requires five parameters to describe the visco-inertial and thermal dissipative effects that operate within porous media. The five non-acoustical physical parameters are: flow resistivity σ, porosity ϕ, tortuosity α_∞, viscous characteristic length (VCL) Λ, and thermal characteristic length (TCL) Λ'. The outputs of the JCA model are complex density, $\tilde{\rho}$, and complex bulk modulus, $\tilde{B}$: i.e.,

$$\tilde{\rho}(\omega) = \frac{\alpha_\infty \rho_o}{\phi}\left[1 + \frac{\sigma\phi}{j\omega\rho_o\alpha_\infty}\sqrt{1 + j\frac{4\alpha_\infty^2\eta\rho_o\omega}{\sigma^2\Lambda^2\phi^2}}\right] \tag{3}$$

$$\tilde{B}(\omega) = \frac{\gamma P_o/\phi}{\gamma - (\gamma - 1)\left[1 + j\dfrac{8\kappa}{\Lambda'^2 C_p\rho_o\omega}\sqrt{1 + j\dfrac{\Lambda'^2 C_p\rho_o\omega}{16\kappa}}\right]} \tag{4}$$

where ρ_o is the air density, η is the air kinematic viscosity, γ is the fluid specific heat ratio, C_p/C_v, C_p is the heat capacity at a constant pressure, C_v is the heat capacity at a constant volume, and κ is the thermal conductivity. Figure 2.4 summarizes the comparison between the DBM model and the JCA model. The decision to use the JCA model was based on the observation that the DBM model places limitations on the range of the flow resistivity (FR) design parameter, as shown in

Figure 1.12, which displays the available boundary of the FR for each propagation model under the same frequency range of interest. The DBM model results in a negative real part of the complex density above a certain FR, which is a non-physical result. Consequently, that model has a restricted boundary on its design parameter. To explore a wider range of design parameters, the JCA model was employed in this research.

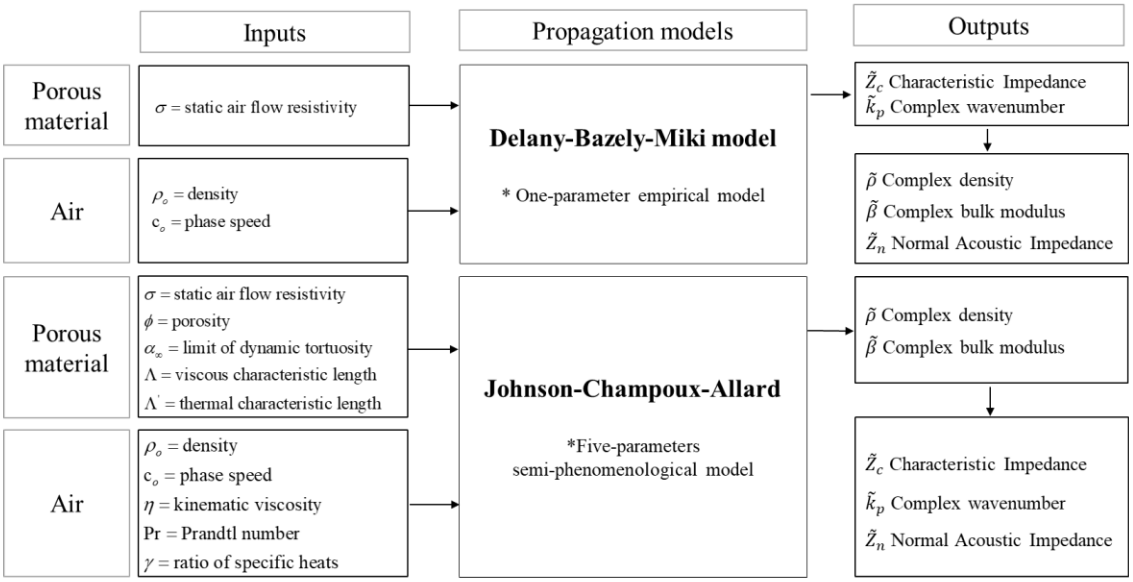

Figure 2.4. Sound propagation models in a porous material (DBM and JCA)

2.4 Acoustic Model of a Two-dimensional Lined Tire

2.4.1 Theoretical Analysis

A two-dimensional lined duct was constructed theoretically to investigate the frequency reduction and attenuation of the tire cavity mode in a lined tire. Figure 2.5 shows a schematic diagram of the two-dimensional duct lined with a porous layer. For this study, the tire size of 235/50R18 was selected. The length of the duct was assumed to be equivalent to the average circumference of the tire cavity, 1.669 m, to ensure that the first duct cavity mode occurs at the first modal frequency of the tire cavity. The wavenumbers were computed from the governing equation and boundary conditions to analyze the effect of the porous layer. An extended reaction case [29], which assumes that sound propagates axially in both the air layer and porous layer, was used in the theoretical derivation.

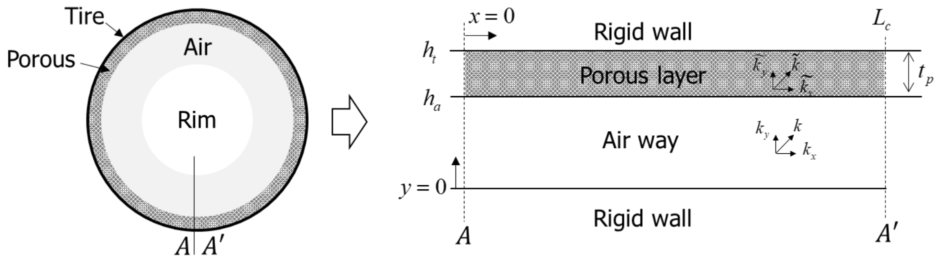

Figure 2.5. Schematic of the two-dimensional duct lined with a porous layer.

The wave equation governing sound propagation in the air cavity of the lined tire is the Helmholtz equation,

$$\nabla^2 p_o + k^2 p_o = 0 \tag{5}$$

where $k = \omega/c$ denotes the wavenumber, c represents the sound speed, and ω represents the angular frequency. The acoustic pressure distributions within the tire in the airway, p_o, and within the porous material, $\tilde{p}$, are expressed as follows:

$$\begin{aligned} p_o &= \left(Ae^{jk_y y} + Be^{-jk_y y}\right)e^{-jk_x x}e^{j\omega t} \\ \tilde{p} &= \left(Ce^{j\tilde{k}_y y} + De^{-j\tilde{k}_y y}\right)e^{-j\tilde{k}_x x}e^{j\omega t}. \end{aligned} \tag{6}$$

The constants *A* to *D* express the complex amplitudes of the waves and the axial and transverse wavenumbers in the airway are represented as k_x and k_y, respectively, while the corresponding values in the porous layer are denoted as $\tilde{k}_x$ and $\tilde{k}_y$, respectively. The relationship between the wavenumbers is expressed as

$$k_x^2 + k_y^2 = k^2 \quad \text{and} \quad \tilde{k}_x^2 + \tilde{k}_y^2 = \tilde{k}^2. \tag{7}$$

2.4.2 Boundary Condition

The duct boundary conditions can be written as

$$\begin{aligned} u_o|_{y=0} &= -\frac{1}{j\omega\rho_o}\frac{\partial p_o}{\partial y} = 0 \\ \tilde{u}|_{y=h_t} &= -\frac{1}{j\omega\tilde{p}}\frac{\partial \tilde{p}}{\partial y} = 0 \\ u_o|_{y=h_a^-} &= \tilde{u}|_{y=h_a^+} \end{aligned} \tag{8}$$

$$p_o|_{y=h_a^-} = \tilde{p}|_{y=h_a^+}$$

where the normal particle velocity in the airway and within the porous layer are represented as u_o and $\tilde{u}$, respectively. Rigid boundary conditions apply at the top and bottom of the duct, causing the particle velocity to be zero at those locations. Continuity of pressure and normal particle velocity are defined at the interface between the airway and porous layer. As a result of applying the boundary conditions, the following transcendental equation that can be solved for the axial wavenumber was obtained: i.e.,

$$-\tilde{\rho}\sqrt{k^2 - k_x^2}\tan\left(h_a\sqrt{k^2 - k_x^2}\right) = \rho_o\sqrt{\tilde{k}^2 - \tilde{k}_x{}^2}\tan\left(t_p\sqrt{\tilde{k}^2 - \tilde{k}_x{}^2}\right) \tag{9}$$

where $\tilde{\rho}$ is the complex density in the porous layer. A MATLAB function “vpasolve” was used to numerically compute the axial wavenumber, k_x, which is assumed to be the same in both the airway and the porous layer: i.e., it is assumed that $k_x = \tilde{k}_x$.

2.5 Integration of Propagation Model with the Acoustic Modeling of the Lined Tire

The analysis of the effects of a porous lining requires an analysis of the axial wavenumber in the airway direction. This is because the axial wavenumber, k_x, which can be calculated through integration of the JCA model within the acoustic model, determines the cavity frequency and pressure distribution in the tire cavity, as expressed in Equation (6). By using the complex density, $\tilde{\rho}$, and complex bulk modulus, $\tilde{B}$, that are output from the JCA model, Equation (9), can be used to find the complex axial wavenumber in the airway: i.e.,

$$k_x = \beta - j\alpha. \tag{10}$$

In Equation (10), β is the real part, and α is the imaginary part of the axial wavenumber. Note that β determines the first cavity resonance frequency when the relationship between the axial wavenumber and the circumferential length can be expressed as

$$\beta L_c = 2\pi, \tag{11a}$$

or alternatively,

$$\frac{2\pi f_1}{c_{ph}} L_c = 2\pi \tag{11b}$$

where f_1 is the cavity resonance frequency, and c_{ph} is the speed of wave propagating within the airway. In addition, α represents the rate of pressure attenuation along the duct. To investigate the effect of the design parameters on k_x, sixteen different cases and two thicknesses of porous material were considered in this research. Among these cases, eight involved high flow resistivity and were within the extended design boundary made possible by using the JCA model. The behaviors of both the first cavity frequency and the imaginary part of k_x with respect to the change in the design parameters are shown in Figure 2.6. The imaginary part of k_x indicates the attenuation performance for the TACR, with a larger negative value indicating a greater attenuation effect. Table 2.2 summarizes the changes in the design parameters and the theoretical results.

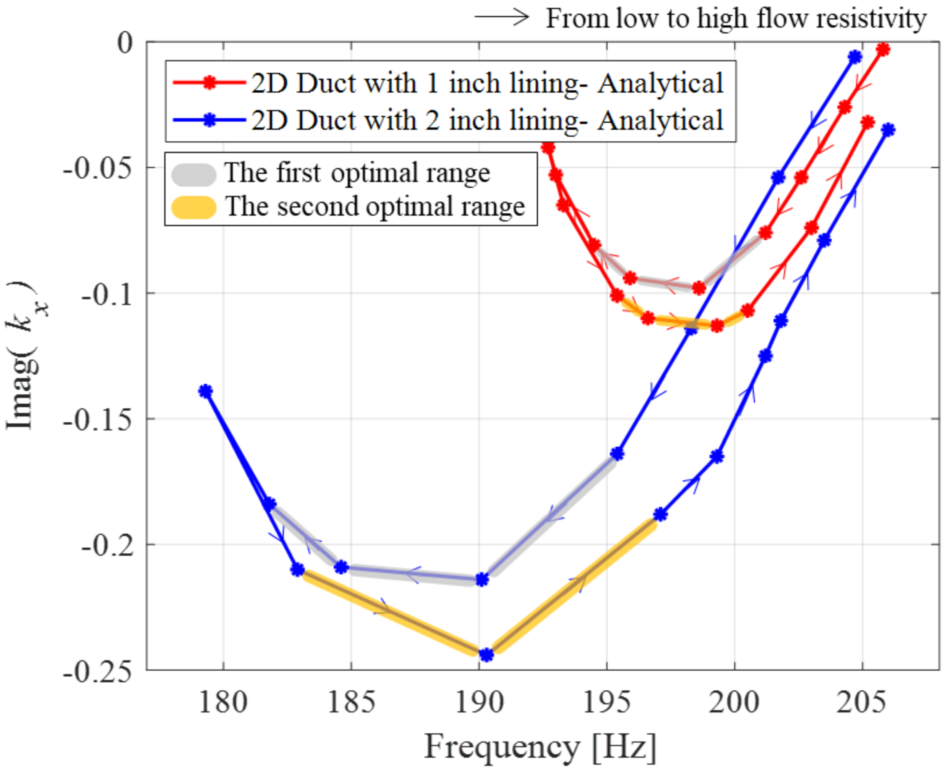

Figure 2.6. Behaviors of the first cavity frequency and the imaginary part of k_x with respect to the change in the flow resistivity.

An increase of the flow resistivity (FR) from a low value leads to a decrease in the first cavity frequency and an increase in the mode attenuation effect. As an example, in the 2 inch case, the first optimal range occurs at a FR of approximately 2,000 Rayls/m. Beyond that value, the cavity frequency continues to decrease, but the attenuation performance deteriorates. An inflection point is observed at a FR of approximately 10,000 Rayls/m. As the FR is increased beyond the inflection point, the cavity frequency increases, but the mode attenuation improves again, forming a second optimal range at around 100,000 Rayls/m. After the second optimal range, the cavity frequency continues to increase while the mode attenuation deteriorates as the FR is further increased. Note that the axial phase speed, c_{ph}, reaches a local minimum in each of the optimal range.

The theoretical analysis thus reveals that the presence of a porous lining results in the axial wavenumber, k_x, being a complex value. The real and imaginary parts of the axial wavenumber determine the behavior of the cavity frequency and attenuation of the TACR. Moreover, the study identified the existence of a second optimal range at a higher FR range, which has not previously been explored because of the limitations of the DBM model. This second optimal range exhibits superior performance compared to the first optimal range in terms of mode attenuation.

Table 2.2. Theoretical results from the integration of the JCA model and acoustic modeling.

Design Parameters			1 inch			2 inch		
σ [Rayls/m]	Λ' [μm]	Λ [μm]	Imag(k_x)	Real(f_1) [Hz]	c_{ph} [m/s]	Imag(k_x)	Real(f_1) [Hz]	c_{ph} [m/s]
0	-	-	0	207	345.6	0	207	345.6
1	18784	10708	-0.003	205.8	343.6	-0.006	204.7	341.7
100	1878	1070	-0.026	204.3	341.1	-0.054	201.7	336.7
500	840	478	-0.054	202.6	338.2	-0.114	198.3	331.0
1,000	594	338	-0.076	201.2	335.9	-0.164	195.4	326.2
2,000	420	239	-0.098	198.6	331.5	-0.214	190.1	317.4
3,500	317	181	-0.094	195.9	327.0	-0.209	184.6	308.2
5,000	265	151	-0.081	194.5	324.7	-0.184	181.8	303.5
10,000	187	107	-0.053	193	322.2	-0.139	179.3	299.3
50,000	84	47	-0.042	192.7	321.7	-0.21	182.9	305.3
100,000	59	34	-0.065	193.3	322.7	-0.244	190.3	317.7
200,000	42	24	-0.101	195.4	326.2	-0.188	197.1	329.0
250,000	37	21	-0.110	196.6	328.2	-0.165	199.3	332.7
400,000	29	17	-0.113	199.3	332.7	-0.125	201.2	335.9
500,000	26	15	-0.107	200.5	334.7	-0.111	201.8	336.9
1,000,000	18	10	-0.074	203	338.9	-0.079	203.5	339.7
5,000,000	8	5	-0.032	205.2	342.6	-0.035	206	343.9

3. FINITE ELEMENT ANALYSIS OF A LINED TIRE

3.1 Introduction

In the work described in this chapter, the frequency reduction and attenuation of the tire cavity resonance were analyzed using a finite element model. The results obtained from the finite element analysis were compared with those obtained from the theoretical analysis presented in Chapter 2 to validate the findings. The simulation involved numerically computing sixteen different cases with varying design parameters to analyze the impact of those parameters on the attenuation of sound pressure inside the tire model and the corresponding frequency reduction. Finally, dispersion diagrams were plotted to illustrate the mechanism of the frequency reduction and attenuation of the tire cavity.

3.2 Verification of Finite Element Method

To verify the finite element method for a porous material, a finite element model was created to emulate the standing wave tube experiment and to calculate the specific normal acoustic impedance of the porous material. Prior to the simulation, a theoretical model was constructed to calculate the specific normal acoustic impedance of the porous material, as shown in Figure 3.1. Based on the assumption of a plane wave excitation from the top of the tube, pressure distribution, $\tilde{p}(x)$, and particle velocity, $\tilde{u}(x)$, in the standing wave tube were expressed as

$$\begin{gathered}\tilde{p}(x) = Ae^{-jkx} + Be^{+jkx} \\ \tilde{u}(x) = \frac{A}{\rho_o c}e^{-jkx} - \frac{B}{\rho_o c}e^{+jkx}.\end{gathered} \tag{12}$$

From Equation (12), the specific normal acoustic impedance, $\tilde{z}_n(x)$, was calculated as:

$$\tilde{z}_n(x) = \frac{\tilde{p}(x)}{\tilde{u}(x)} = \rho_o c\,\frac{Ae^{-jkx} + Be^{+jkx}}{Ae^{-jkx} - Be^{+jkx}} \tag{13}$$

where *A* and *B* are the complex amplitudes of plane waves propagating in the positive and negative going directions, respectively. For the case of a finite depth air layer backed by a rigid surface, *A* and *B* are equal based on the assumption of perfect reflection owing to the rigid backing boundary condition. Hence, the specific normal acoustic impedance of a layer of depth, *d*, can be simplified to

$$\tilde{z}_n(d) = \rho_o c \, \frac{e^{-jkd} + e^{+jkd}}{e^{-jkd} - e^{+jkd}} = -j\rho_o c \cot(kd) \tag{14}$$

in the case of an air layer. For a layer of porous material, the result becomes

$$\tilde{z}_n = -j\omega \frac{\tilde{\rho}}{\tilde{k}} cot\left(\tilde{k}d\right). \tag{15}$$

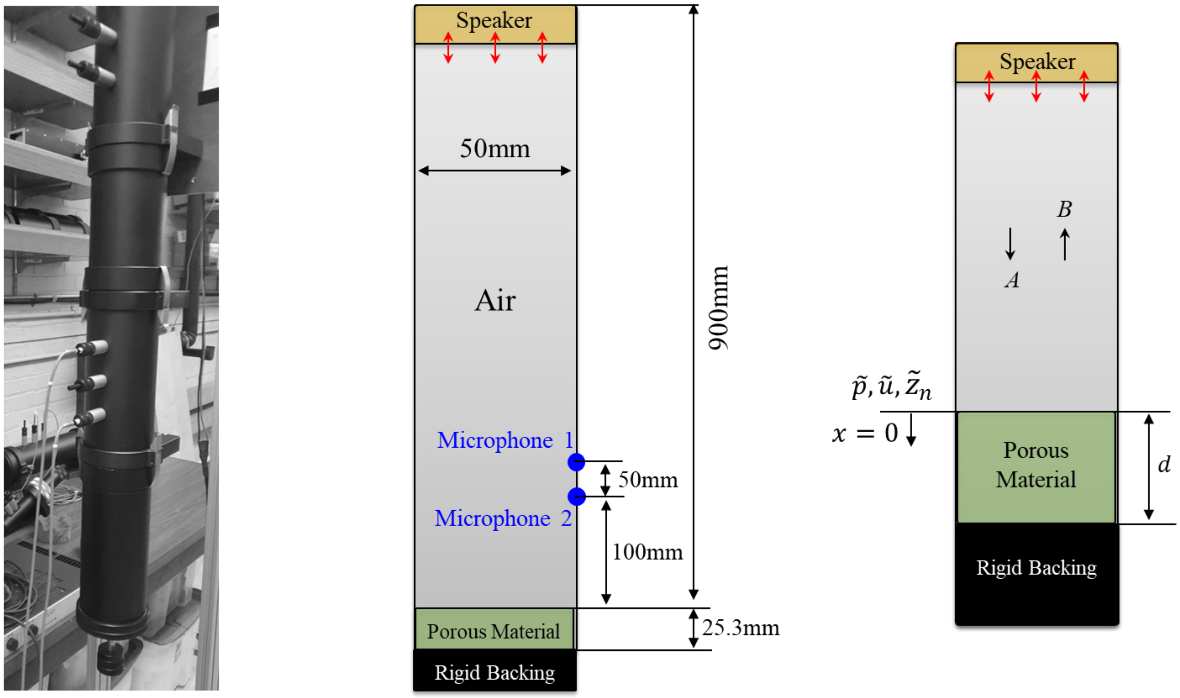

(a) Standing Wave Tube (b) Finite Element Model (c) Theoretical Model

Figure 3.1. Schematic of the standing wave tube for finite element and theoretical model to describe measurement of acoustic properties of porous material.

The finite element model emulates the standing wave tube and is filled with air. A one inch (25.3 mm) porous material is placed at the bottom of the tube, backed by the rigid termination boundary condition. The tube diameter is a 50 mm and the height is 900 mm, excluding the porous material thickness. In addition, two microphones with a 50 mm spacing are placed 100 mm distant from the porous material. A plane acoustic wave of one Pascal is imposed at the top of the model, and the pressures at microphones 1 and 2 are measured to calculate the specific normal acoustic impedance.

In terms of material properties, the bulk modulus of air is 138,710 Pa, measured at 24 deg.C of ambient temperature, which corresponds to the same conditions as the experimental measurement in Chapter 4.1. The density of air is 1.1615 kg/m^3, measured at 99.25 kPa ambient pressure. The porous material properties are frequency-dependent complex density and bulk modulus, both of which are computed by the JCA model and then input to the simulation via the Abaqus input file.

Regarding boundary conditions, the entire tube surface except for the excitation location is modeled as rigid. To ensure interaction between the air (acoustic) and porous material (acoustic), the "TIE" function is applied to create continuity boundary conditions. Figure 3.2 illustrates the comparison between theoretical results, calculated using Equation (15), and the FEA results. It shows good agreement in the frequency range of interest, which indicates the validity of the finite element method of porous material in Abaqus.

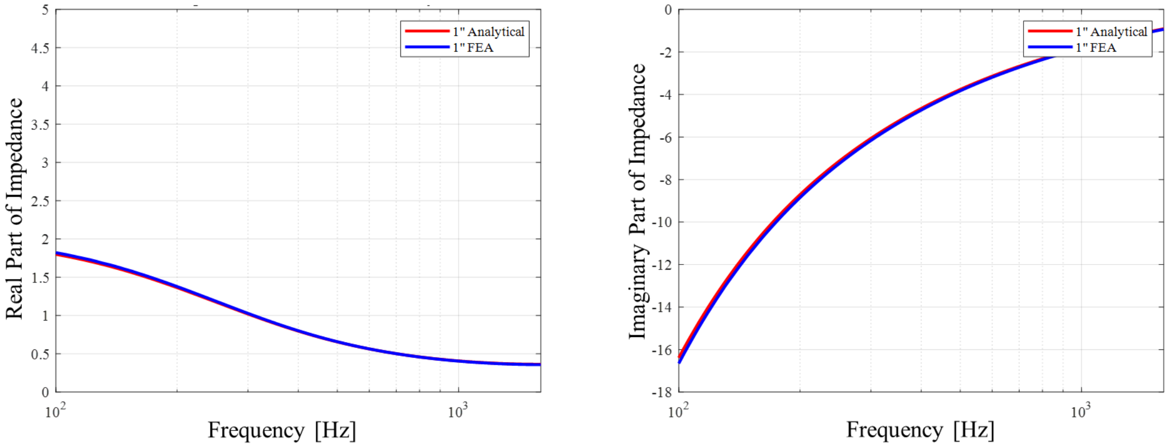

Figure 3.2. Comparison of acoustic impedance between theoretical result and FEA result with 3,500 Rayl/m of FR.

3.3 Finite Element Analysis of the Two-dimensional Torus-shaped Lined Tire

3.3.1 Model Description

To investigate the pressure distribution inside a porous material lined tire and the acceleration at the center of the rim, a tire model consisting of a rim, an air cavity, and a porous layer was constructed. For the component type, a 2D deformable solid was used to create the rim model based on the 18-inch outer diameter size. Similarly, the air cavity model was created as a 2D deformable acoustic medium, with the circumferential length of the cavity matched to the first cavity frequency of the actual tire. Finally, a porous lining with a thickness of either 1 inch or 2 inches was constructed using the 2D deformable acoustic medium. These components were then assembled to form a complete system, and the relationship between them will be explained in detail in the following section.

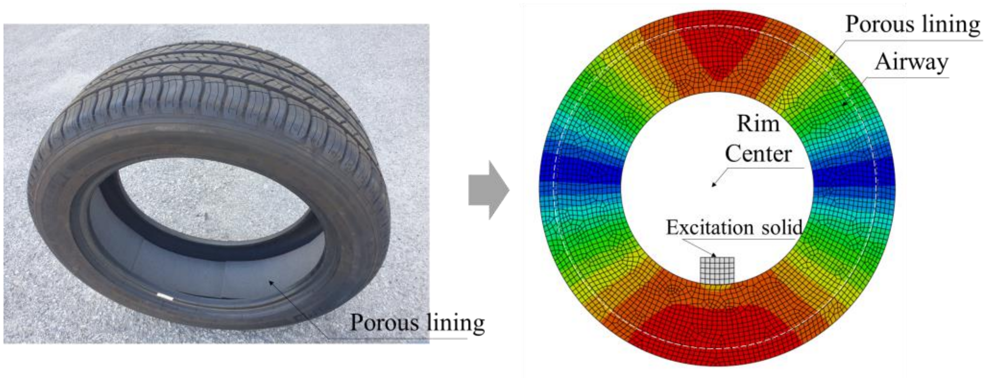

Figure 3.3. Finite Element Model of a lined tire.

The material properties of the rim, air, and porous material are summarized in the Table 2.1. The bulk modulus of air was measured at 24◦C and 99.25 kPa, which corresponds to the same conditions as the experimental measurement. The speed of sound was also calculated to be 345.57 m/s at this temperature. To prevent any interference from rim resonance, the rim's stiffness was set to an exceptionally high value, and its density was adjusted to match that of steel. In particular, the porous material properties are frequency-dependent complex values using the JCA model.

Table 3.1. Summary of material properties in the FEA.

Part	Material type	Density [kg/m^3]	Modulus	Poisson's ratio
Rim	Solid	7850	2e+11 (Elastic)	0.3
Air	Acoustic medium	1.1615	138,710 (Bulk)	-
Porous Material	Acoustic medium	Complex Density $\tilde{\rho}$ from JCA model (Frequency dependent)	Complex Bulk Modulus $\tilde{B}$ from JCA model (Frequency dependent)	-

Regarding the boundary conditions, the rim was immobilized by constraining three degrees of freedom for displacement and three degrees of freedom for rotation. To ensure that all three components of the assembly worked together, continuity constraints were imposed to link each part. To be more specific, the "TIE" function was used to create a continuity boundary condition for two interfaces, namely the interface between air and the rim, and the interface between air and the porous layer. For the “TIE” function between air (acoustic) and rim (stress), the translations on the interface were tied as degrees of freedom. For the interface between air (acoustic) and porous layer (acoustic), the tied degrees of freedom were the acoustic pressure. In both cases, air was designated as the master surface, while the rim and porous layer were set as slaves. Finally, to replicate the impact of road conditions, an excitation solid element was created to function as the source, as illustrated in Figure 3.3. This element was linked to the airway instead of a porous layer to prevent any potential impact from the layer. A “TIE” function was also used to connect the excitation solid and airway. To create the source, a harmonic force of 1 N was applied to the solid component across the desired frequency range.

3.3.2 Simulation Process

There are a total of three steps involved in this simulation, as illustrated in Figure 3.4. In the first step, an input file is generated for the simulation. Based on the tire model described in Section 3.2.1, a steady-state dynamic direct method is set up to compute the complex response of pressure and acceleration in the frequency range of 100-500 Hz. In the second step, the input file is modified to include the properties of the porous material. These properties are calculated using the JCA model with respect to varying design variables and frequencies. Finally, the simulation is executed using the Abaqus Command and the results are visualized in the Abaqus CAE. The complex sound pressure along the tire air cavity, which is an output of the simulation, is then extracted from Abaqus and imported to MATLAB to plot the sound pressure level and dispersion diagrams. Figure 3.5 shows the location of the microphone where the sound pressure level was computed from the simulation. The first cavity frequency and the peak value of sound pressure level at that frequency were obtained from the sixteen different cases of simulation for two different thickness of porous layers. These results will be compared with the theoretical results and will be discussed in further detail in Section 3.4. Additionally, to evaluate the effect of porous linings on the acceleration transmissibility, the inertance at the rim center, described in Figure 3.3, was also measured. The simulation was conducted with two thicknesses of porous layer with 3,500 Rayls/m of FR. These results will be validated by comparison with the experimental results in Section 4.2.

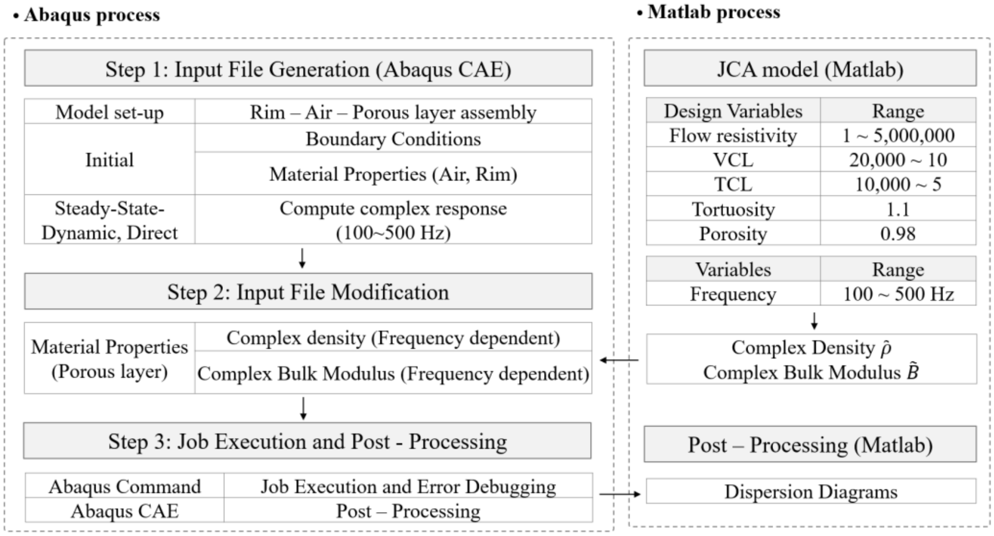

Figure 3.4. Finite Element Analysis process for a porous lined tire.

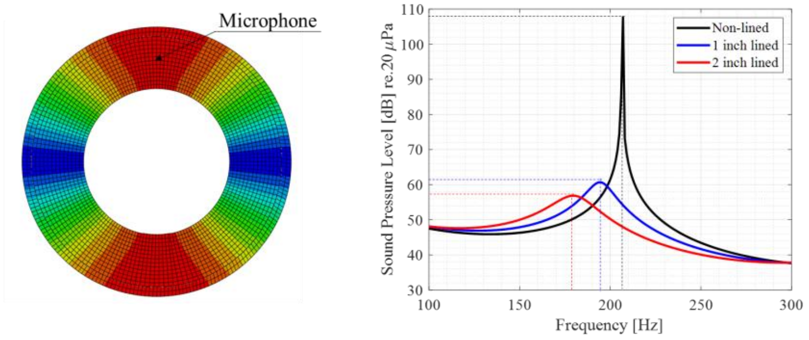

(a) Microphone location (center of airway)

(b) Sound Pressure Level at the microphone location

Figure 3.5. Sound Pressure Level at microphone location from FEA with 3,500 Rayl/m of FR.

3.4 Results and discussion

The finite element analysis of the lined tire involved extracting the tire cavity resonance frequency and sound pressure level at that frequency. These simulation results are compared with those obtained from the theoretical work in Figure 3.6 and Table 3.2. Overall, the simulation results showed a similar pattern to that observed in the theoretical work. The design cases that produced a larger negative imaginary part of the axial wavenumber were validated by the lower sound pressure level in the FE simulation, indicating improved mode attenuation. Furthermore, it was observed that the design cases within the second optimal range from the simulation matched those from the theoretical work. Regarding the cavity frequency prediction, the maximum errors were 0.9% and 2.9% for the 1 and 2 inch thicknesses, respectively.

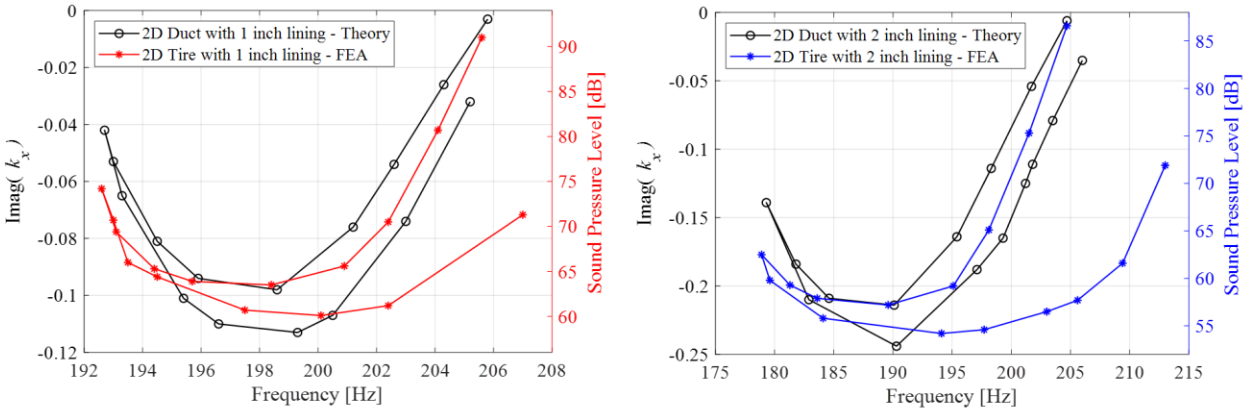

(a) 1 inch porous lining

(b) 2 inch porous lining

Figure 3.6. Behavior of first cavity frequency and sound pressure level from theory and FEA.

Additionally, smaller errors were observed for the low FR cases, while larger errors were observed for the high FR cases. In particular, at very high FR values, the frequency reached the original value or even became higher. This effect occurred because the porous material behaved as if it were a solid due to the very high FR. The “solid” porous layer caused the circumferential length of the air cavity to be shortened, resulting in a higher tire cavity frequency. This trend was more pronounced in the 2 inch cases.

Figure 3.7 illustrates the relationship between mode attenuation and flow resistivity in the 2 inch lined tire cases. As the flow resistivity increases from a low value and reaches its first optimal range of 2,000 Rayls/m, the sound pressure level decreases to 57.2 dB from its original value of 107.6 dB in the non-lined case. However, as the flow resistivity continues to increase to 10,000 Rayls/m, the attenuation deteriorates, and the sound pressure level increases to 62.5 dB. By further increasing the flow resistivity up to 200,000 Rayls/m, which is the second optimal range, the sound pressure level is reduced to 54.2 dB, which is the minimum level of attenuation observed in this study. Beyond the second optimal range, further increases in flow resistivity worsen the attenuation. Interestingly, at very high flow resistivities of around 5,000,000 Rayls/m, the first cavity frequency increases to 213 Hz, which is even higher than the original first cavity frequency. As previously explained, this is due to the porous layer becoming like a solid, resulting in a shorter circumferential length of the tire.

Table 3.2. Comparison between the theoretical and the numerical results.

Design Parameters			1 inch				Error of Real(f_1)	2 inch				Error of Real(f_1)
			Theory		FEA			Theory		FEA		
σ [Rayls/m]	Λ' [μm]	Λ [μm]	Imag(k_x)	Real(f_1) [Hz]	SPL [dB]	Real(f_1) [Hz]		Imag(k_x)	Real(f_1) [Hz]	SPL [dB]	Real(f_1) [Hz]	
0	-	-	0	207.0	94	207.0	-	0	207.0	107.6	207.0	-
1	18,784	10,708	-0.003	205.8	91.0	205.6	-0.1%	-0.006	204.7	86.6	204.7	0.0%
100	1,878	1,070	-0.026	204.3	80.7	204.1	-0.1%	-0.054	201.7	75.3	201.5	-0.1%
500	840	478	-0.054	202.6	70.5	202.4	-0.1%	-0.114	198.3	65.1	198.1	-0.1%
1,000	594	338	-0.076	201.2	65.6	200.9	-0.1%	-0.164	195.4	59.2	195.1	-0.2%
2,000	420	239	-0.098	198.6	63.5	198.4	-0.1%	-0.214	190.1	57.2	189.6	-0.3%
3,500	317	181	-0.094	195.9	63.9	195.7	-0.1%	-0.209	184.6	57.9	183.6	-0.5%
5,000	265	151	-0.081	194.5	65.3	194.4	-0.1%	-0.184	181.8	59.3	181.3	-0.3%
10,000	187	107	-0.053	193.0	69.4	193.1	0.1%	-0.139	179.3	62.5	178.9	-0.2%
50,000	84	47	-0.042	192.7	74.2	192.6	-0.1%	-0.210	182.9	59.8	179.6	-1.8%
100,000	59	34	-0.065	193.3	70.7	193.0	-0.2%	-0.244	190.3	55.8	184.1	-2.2%
200,000	42	24	-0.101	195.4	66.0	193.5	-0.9%	-0.188	197.1	54.2	194.1	-1.5%
250,000	37	21	-0.110	196.6	64.4	194.5	-0.6%	-0.165	199.3	54.6	197.7	-0.3%
400,000	29	17	-0.113	199.3	60.7	197.5	-0.9%	-0.125	201.2	56.5	203.0	1.4%
500,000	26	15	-0.107	200.5	60.1	200.1	-0.7%	-0.111	201.8	57.7	205.6	2.4%
1,000,000	18	10	-0.074	203	61.2	202.4	-0.4%	-0.079	203.5	61.6	209.4	2.9%
5,000,000	8	5	-0.032	205.2	71.3	207	0.9%	-0.035	206.0	71.9	213.0	2.4%

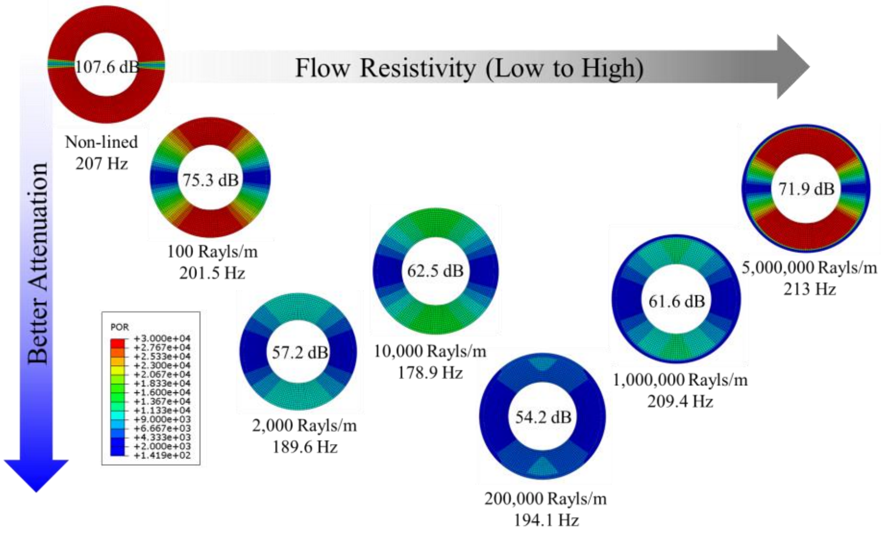

Figure 3.7. Behavior of mode attenuation with respect to change in flow resistivity.

To highlight the impact of the second optimal range, cases with varying thicknesses but the same level of frequency reduction and mode attenuation are compared in Figure 3.8. The results indicate that a design with a 1.5 inch thickness within the first optimal range and the design with a 1 inch thickness within the second optimal range both achieved a comparable level of sound pressure level to that of the non-optimized acoustic foam with a 2 inch thickness. The results of this case study suggest that by optimizing the design of the porous lining material, it is possible to achieve equivalent levels of attenuation with a thinner thickness of lining material compared to a thicker one.

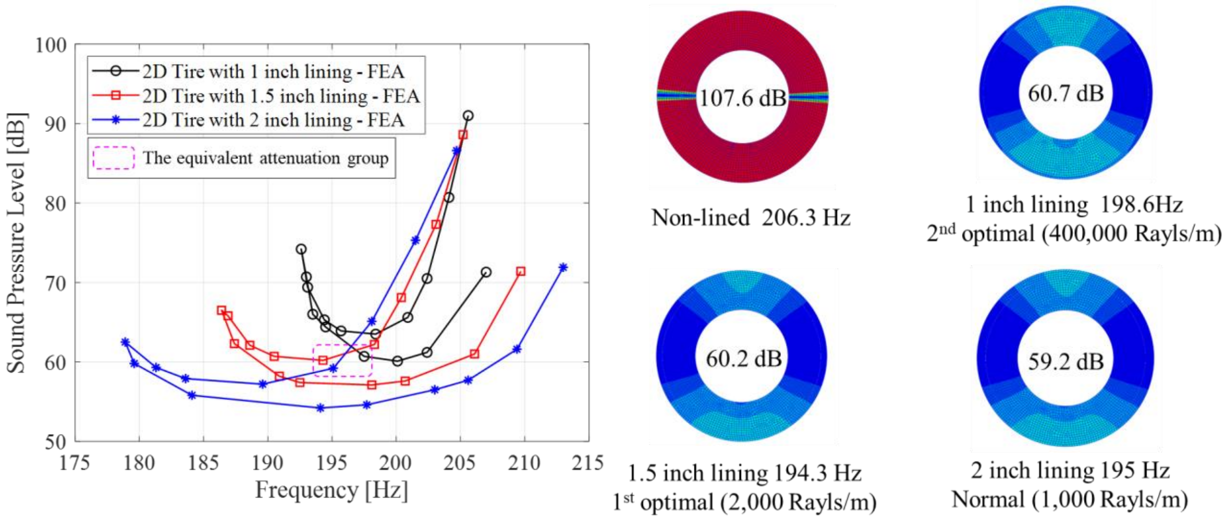

Figure 3.8. Case study of the equivalent level of attenuation with different design.

The dispersion diagram is a graphical representation of a wavenumber decomposition of a propagating wave [30]. In terms of interpretation, the magnitude of the dispersion curve represents the sound pressure level at a particular wavenumber and frequency, while the slope of the curve joining the origin and a point on the dispersion curve indicates the phase speed. To visualize the effect of a porous lining, the dispersion diagram was plotted by extracting sound pressure from the FE results at 170 nodes along the circumference of the tire's air cavity and Fourier transforming that data via MATLAB code.

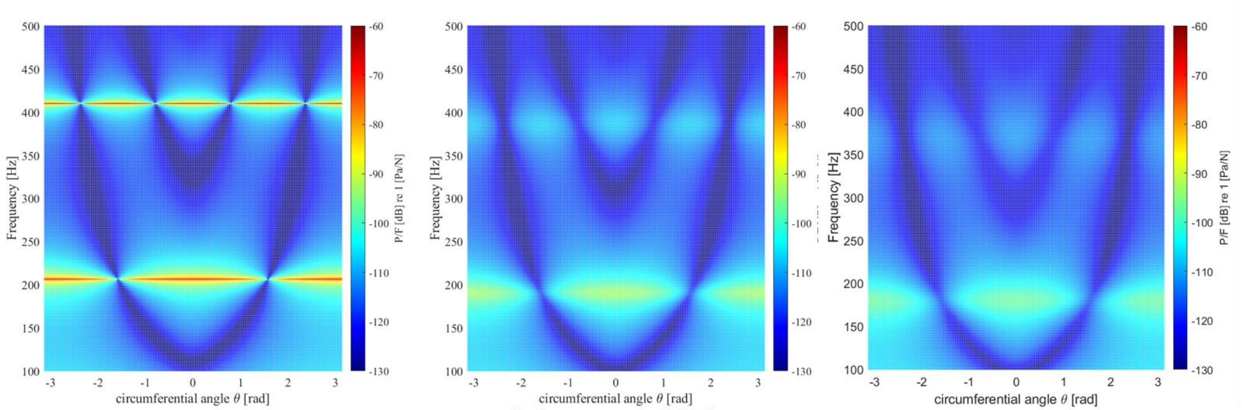

(a-1) Pressure – non-lined (b-1) Pressure – 1 inch lined (c-1) Pressure – 2 inch lined

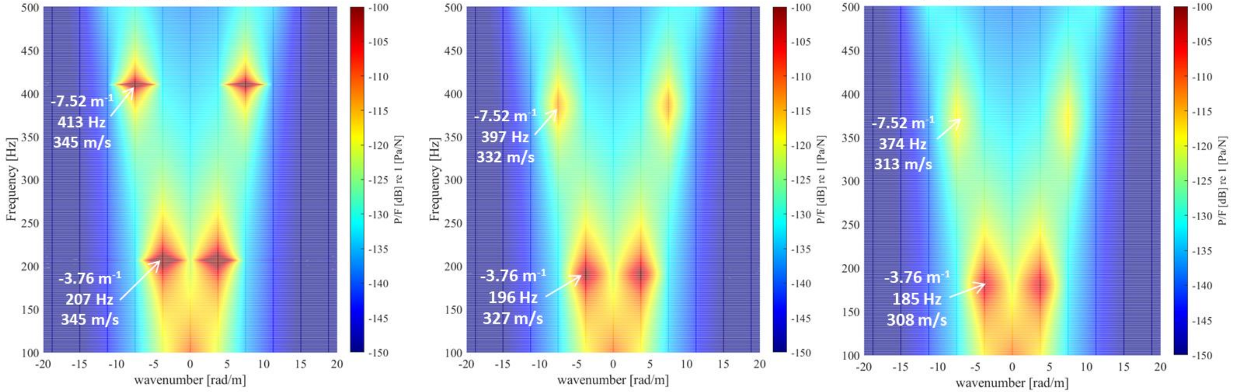

(a-2) Dispersion – non-lined (b-2) Dispersion – 1 inch lined (c-2) Dispersion – 2 inch lined

Figure 3.9. Pressure distribution and dispersion diagram from FEA with 3,500 Rayl/m of FR.

Figure 3.9 displays the pressure distributions along the tire circumference and the dispersion diagrams with respect to wavenumber for both the 1 inch and 2 inch lining cases. The lined cases were simulated based on the FR of 3,500 Rayls/m. The pressure distribution effectively captured the frequency reduction and mode attenuation, while the dispersion diagram showed that the phase speed of the lined tire was slower than that of the non-lined tire. Additionally, it was observed that the phase speed varied depending on the frequency, indicating that the wave type inside the lined tire was dispersive, meaning that different frequency components travel at different speeds.

4. EXPERIMENTAL ANALYSIS: VALIDATION AND APPLICATION

4.1 Measurement of Acoustic Impedance and Design Parameter Estimation

As the first step in experimental validation, the acoustic impedance of an actual sample of acoustic polyurethane foam, a porous material, was measured. A curve-fitting optimization was then conducted using MATLAB software to estimate its design parameters. Figure 4.1 illustrates the entire process of the measurement and curve-fitting optimization.

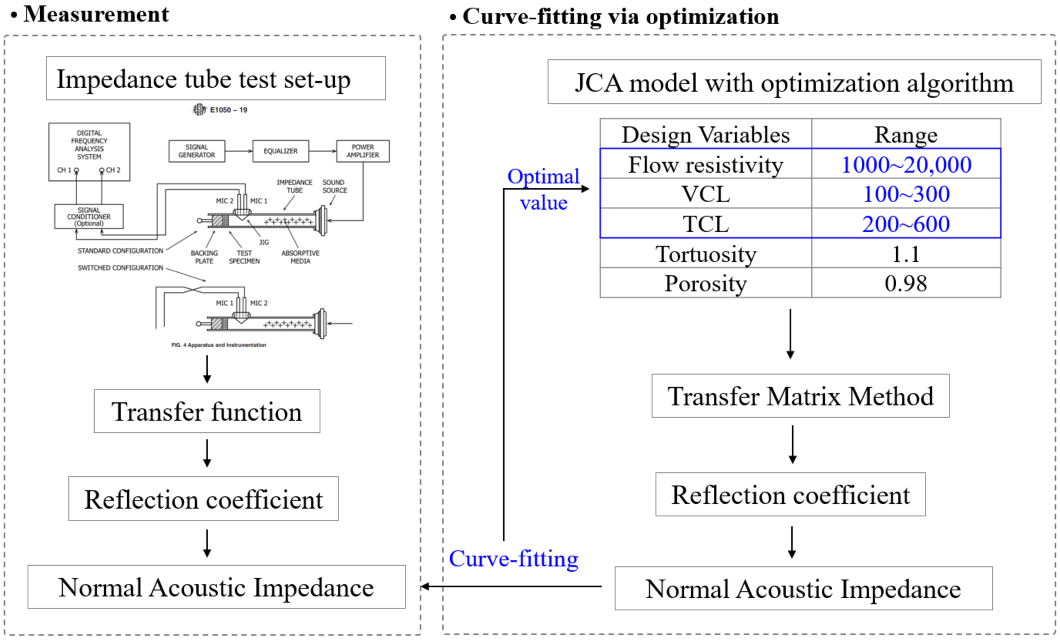

Design Variables	Range
Flow resistivity	1000~20,000
VCL	100~300
TCL	200~600
Tortuosity	1.1
Porosity	0.98

Figure 4.1. Measurement and curve-fitting process of acoustic impedance [31].

A standard Brüel and Kjaer standing wave tube (4206) was used in the measurement process to determine the reflection coefficient and normal acoustic impedance of the porous material sample via the two-microphone method [31]. To conduct the curve-fitting, it was necessary to determine both control and fixed variables. In this study, the control variables were selected to be flow resistivity, VCL, and TCL, while porosity and tortuosity were considered to be fixed variables. Regarding the process, the complex density, $\tilde{\rho}$, and complex bulk modulus, $\tilde{B}$, extracted from the JCA model were used to determine the characteristic impedance, $\tilde{z}_c$, and complex wavenumber, $\tilde{k}_p$: i.e.,

$$\tilde{z}_c = \tilde{\rho}\,\tilde{c} = \sqrt{\tilde{\rho}\,\tilde{B}}$$
$$\tilde{k}_p = \frac{\omega}{\tilde{c}} = \omega\sqrt{\frac{\tilde{\rho}}{\tilde{B}}} \tag{15}$$

where $\tilde{c}$ is the complex speed of sound within the porous material. These values were then input to the transfer matrix for modeling the porous layer, which is based on the assumption that the porous material is rigid and is backed by a rigid termination.

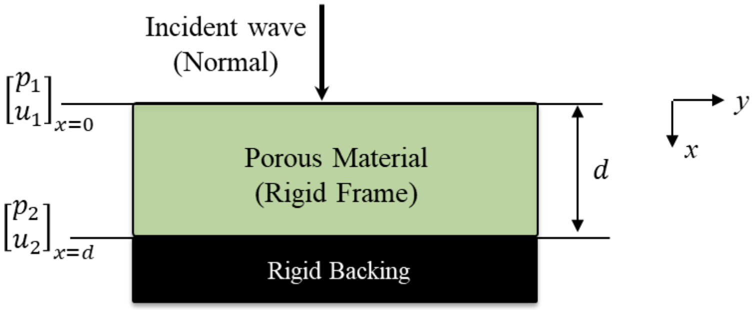

Figure 4.2. The Transfer Matrix Method for a rigid porous layer.

The transfer matrix for modeling the porous layer is

$$\begin{bmatrix} p_1 \\ u_1 \end{bmatrix}_{x=0} = \begin{bmatrix} T_{11} & T_{12} \\ T_{21} & T_{22} \end{bmatrix} \begin{bmatrix} p_2 \\ u_2 \end{bmatrix}_{x=d}$$
$$\text{where } \begin{bmatrix} T_{11} & T_{12} \\ T_{21} & T_{22} \end{bmatrix} = \begin{bmatrix} \cos(\tilde{k}_p d) & j\tilde{z}_c \sin(\tilde{k}_p d) \\ j\frac{1}{\tilde{z}_c}\sin(\tilde{k}_p d) & \cos(\tilde{k}_p d) \end{bmatrix}. \tag{16}$$

The pressure and particle velocity at $x = 0$ and $x = d$ are represented as $p_1,\ u_1$ and $p_2,\ u_2$, respectively. For the rigid backing boundary condition, T_{12} and T_{22} are neglected in calculating the reflection coefficient because the particle velocity, u_2, is zero at $x = d$. The reflection coefficient at normal incidence, R, can be written as

$$R = \frac{T_{11}/(T_{21}\rho_o c) - 1}{T_{11}/(T_{21}\rho_o c) + 1}. \tag{17}$$

Finally, Equation (13) can be used to estimate the specific normal acoustic impedance of porous material: i.e.,

$$\tilde{z}_n = \rho_o c \frac{1 + R}{1 - R}. \tag{18}$$

The estimated acoustic impedance was curve-fitted based on the measured acoustic impedance using a MATLAB optimization function “particleswarm” to identify the optimal value of design variables. Figure 4.5 illustrates the result of the curve-fitting, and the optimized design variables were obtained over the frequency range up to 1.6 kHz. The values obtained are summarized in Table 4.1.

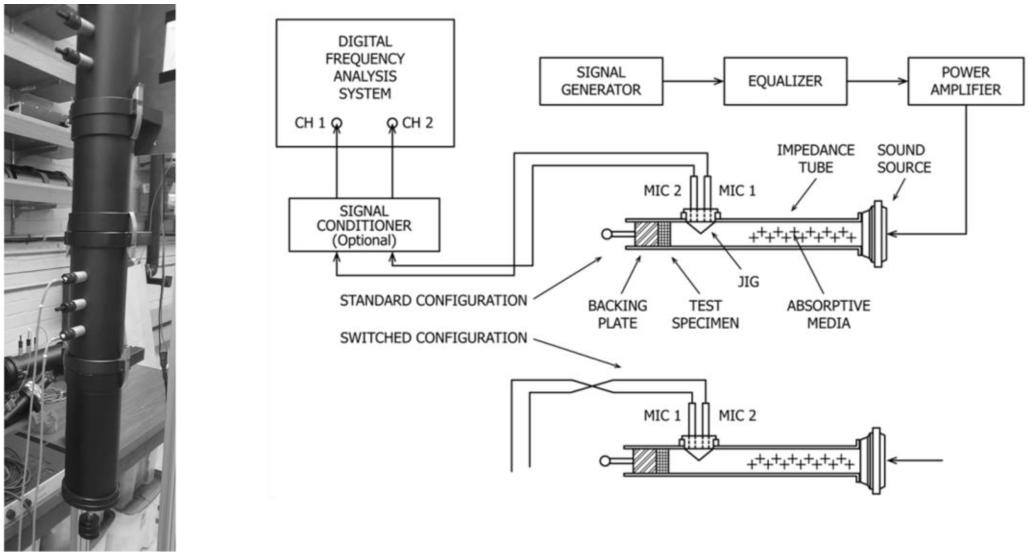

(a) Standing Wave Tube (Type 4206 Large tube)

(b) Apparatus and Instrumentation for the Two Microphone Method

Figure 4.3. Measurement set-up for acoustic impedance of porous material.

Figure 4.4. Sample of porous material provided by Soundcoat for research purposes.

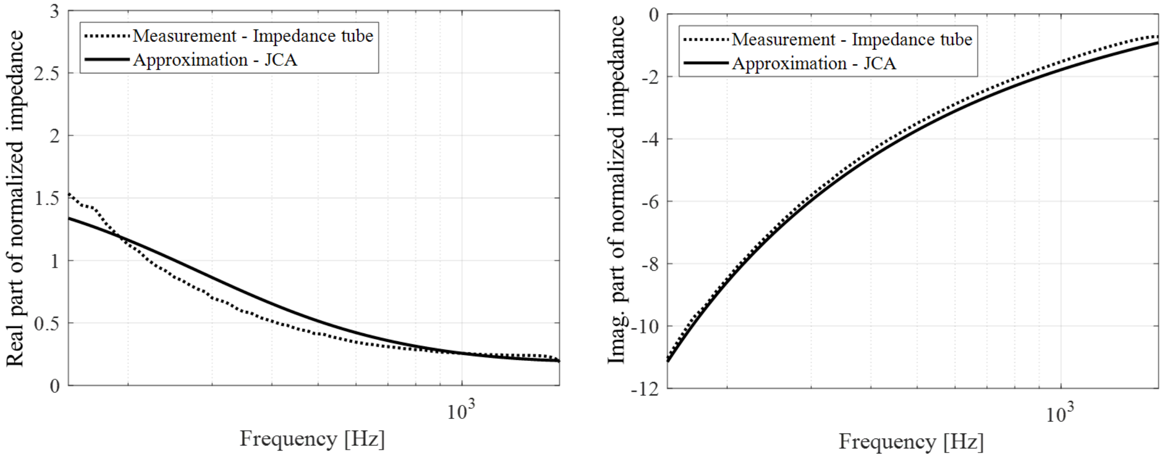

(a) Real part of the normalized surface acoustic impedance

(b) Imaginary part of the normalized surface acoustic impedance

Figure 4.5. Comparison between the measurement and estimation of the acoustic impedance.

Table 4.1. Estimated design parameters of the acoustic polyurethane foam.

Variables	Range	Estimated Value
Flow resistivity [Rayls/m]	1000~20,000	3,500
Viscous Characteristic Length [μm]	100~300	181
Thermal Characteristic Length [μm]	200~600	317
Tortuosity	1.1	1.1
Porosity	0.98	0.98

4.2 Measurement of Acceleration of a Tire under Free Boundary Condition

As the second step in experimental validation, the acceleration of a lined tire under free boundary conditions was measured. The results were then compared with the result obtained in finite element analysis in Chapter 3.3.2 to validate the frequency reduction and mode attenuation achieved through the use of a porous lining. A tire lined with the porous material with a flow resistivity of 3,500 Rayls/m was suspended in the air with a flexible cord while a tri-axial accelerometer was positioned at the wheel center, as depicted in Figure 4.6(b). The tire tread was subjected to vertical excitation using an impact hammer, and the acceleration was measured. The inertance frequency response at the wheel hub center is shown in Figure 4.6(a). The first cavity frequency at 207 Hz was reduced to 198 Hz and 182 Hz, and the peak inertance was also decreased by 16.1 dB and 19 dB in the 1 inch and 2 inch foam lining cases, respectively. These results are in good agreement with that from simulation as summarized in Table 4.2.

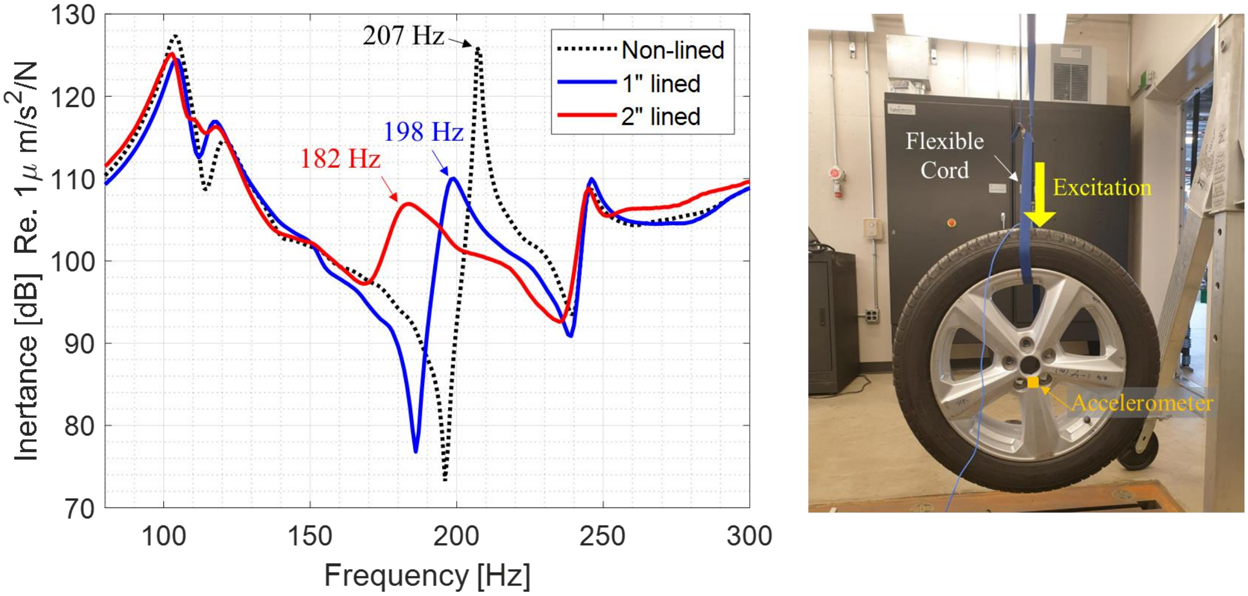

(a) Inertance at the wheel hub center

(b) Free boundary condition

Figure 4.6. Inertance frequency response of non-lined and lined cases under free boundary conditions.

Table 4.2. Comparison between the measurement and the simulation.

Cases	Measurement		Simulation	
	Inertance [dB] Re. 1 $\mu m/s^2/N$	Frequency [Hz]	Inertance [dB] Re. 1 $\mu m/s^2/N$	Frequency [Hz]
Non-lined	125.9	207	122.7	207
1” lined	109.8	198	100.9	195.9
2” lined	106.9	183	97.8	183.6

4.3 Measurement of Transmitted Acceleration of a Static and Loaded Tire

The experimental validation of the effect of porous lining was also conducted under the static and loaded boundary condition. The same lined tire from Chapter 4.2 was fixed at its hub on a static test rig [32] and loaded to 1,000 lbs. A tri-axial accelerometer was positioned at the inner rim, as depicted in Figure 4.7. The center of the tire tread was subjected to an excitation using an impact hammer, and the acceleration was measured.

The results of three cases, non-lined, 1 inch lined, and 2 inch lined, are compared in Figure 4.7 under the loaded boundary condition. Two cavity peaks at 207 Hz and 198 Hz were observed in the non-lined case. The addition of the 1 inch and 2 inch linings decreased the cavity frequency to 196 Hz and 189 Hz, respectively. The inertance peak was also reduced from 104 dB and 113 dB for the two peaks of non-lined cases to 98 dB and 93 dB for the 1 inch and 2 inch lined cases, respectively. These findings indicate that the porous lining has an impact on the frequency reduction and attenuation of tire air cavity resonance.

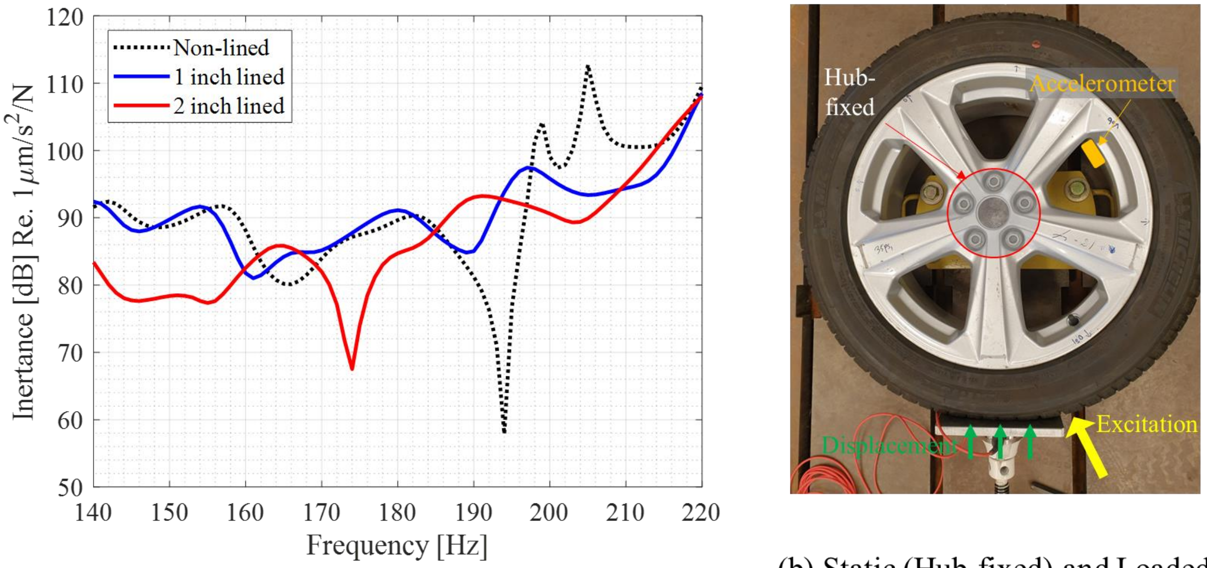

(a) Inertance at the inner rim

(b) Static (Hub-fixed) and Loaded Boundary Condition

Figure 4.7. Inertance frequency response of non-lined and lined cases under static and loaded boundary condition.

4.4 Measurement of Transmitted Force and Internal Sound Pressure of a Rolling Tire

The effect of the porous lining on TACR was validated under tire rolling conditions by measuring the transmitted force and sound pressure inside the tire. This involved placing a force transducer at the hub center and a wireless microphone on the rim while a 235/50R18 Michelin tire was loaded to 1,000 lbs. For the force and sound pressure measurement under rolling conditions, the tire was rolled over the pavement at 30 mph and 10 mph, respectively. To be more specific, as depicted in Figure 4.8, the tire rolling test was conducted using the Tire Pavement Test

Apparatus (TPTA) at the Herrick Laboratories, Purdue University. The main beam can be moved in the radial direction of the rotating disc to load and unload the test tire up to 1,000 lbs, and the rotating disc is operated by an electric motor inside the apparatus to run the tire up to 30 mph along the pavement.

(a) Side View (b) Isometric View

Figure 4.8. Tire Pavement Test Apparatus in Herrick Labs at Purdue University.

The experimental set-up involved mounting a test tire on a specified rim connected to a wheel force transducer, as shown in Figure 4.9. The wheel-tire assembly was then installed on the test rig, and a tri-axial accelerometer was placed on the center of the hub to measure the transmitted acceleration to the suspension. In addition, Figure 4.10 depicts a wireless microphone fixed on the rim (inside the test tire) to measure the internal sound pressure inside the rolling tire. This device was wirelessly controlled, and sound pressure inside the rolling tire was recorded at 10 mph.

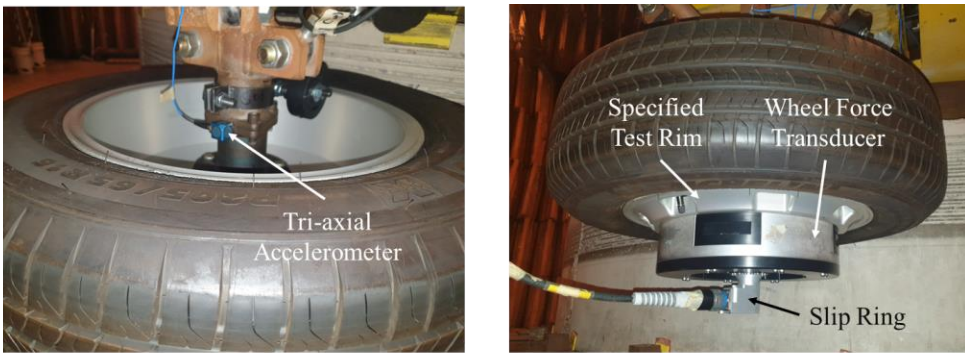

(a) Acceleration Measurement (b) Force and Moment Measurement

Figure 4.9. Accelerometer and wheel force transducer.

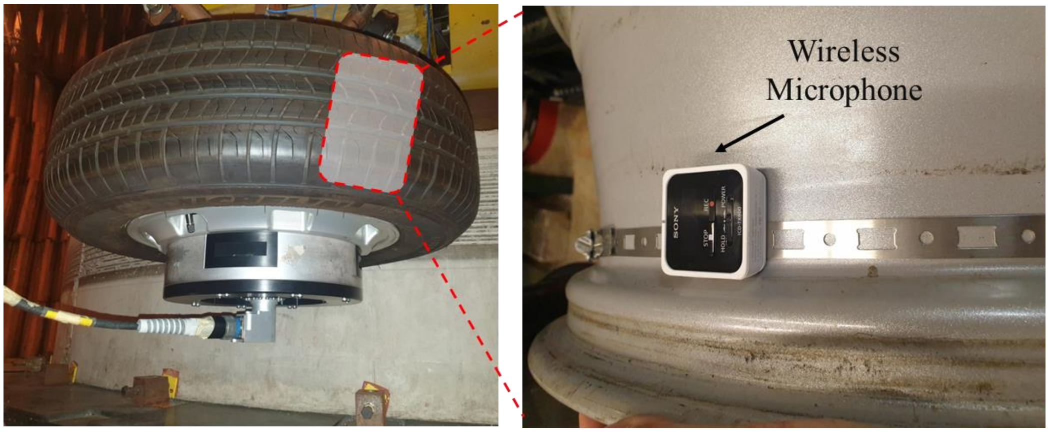

Figure 4.10. Wireless microphone installed on the rim inside a tire.

Figure 4.11 shows the measurement and analysis process for the experiments conducted under rolling boundary conditions. The force, moment, and acceleration data collected in the experiments were sent to the Brüel and Kjaer (B&K) Pulse software on a laptop via a wifi router. The time domain signals were recorded for processing in B&K Pulse and were analyzed later using MATLAB code. Additionally, the internal pressure measured by the wireless microphone on the rolling rim was provided to the B&K Connect software, and spectrogram analysis was conducted using that software.

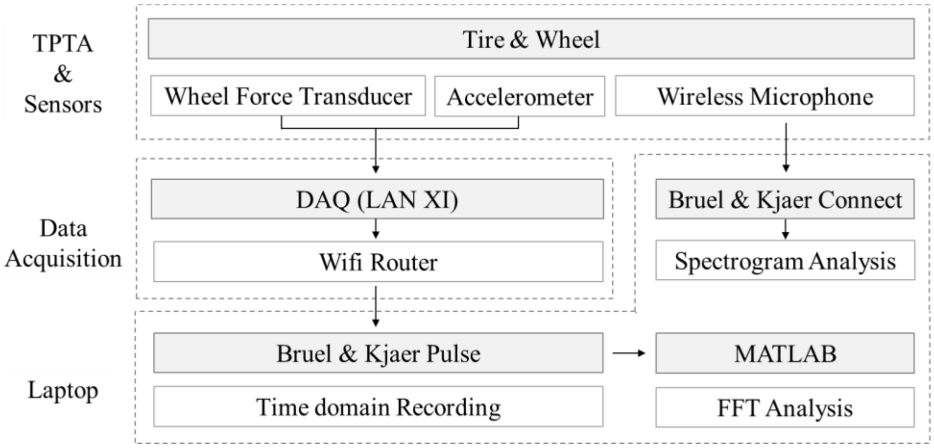

Figure 4.11. Measurement and analysis procedure in the rolling tire experiment.

The acceleration, force, and moment measured at the wheel center location are compared between the non-lined tire case and the lined tire case, as shown in Figure 4.12. These results confirmed the effectiveness of the porous lining, with approximately a minimum of 10 dB and a maximum of 15 dB reduction in the six different directions of measurement. The explanation of each direction can be found in the Appendix. Regarding the frequency reduction, although it was not very clear in all measurements, a frequency reduction of 10 Hz was captured in Figure 4.12 (a), (c), (d), and (f), as expected in the theoretical and finite element analysis. One possible explanation for the unclear frequency reduction in all directions is due to the skewed angle of cavity resonance under rolling boundary condition, where the tire's acoustic mode is deflected about 30-60° depending on the speed.

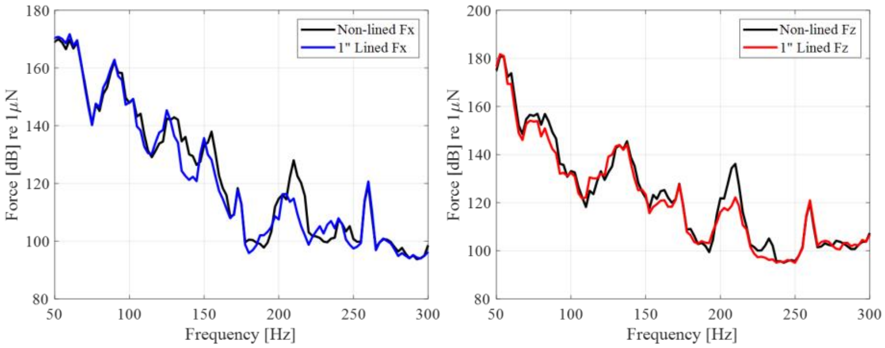

(a) Longitudinal Force at 30 mph (b) Vertical Force at 30 mph

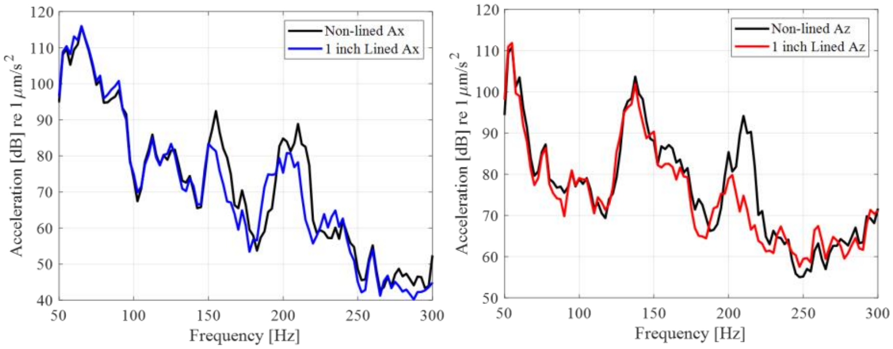

(c) Longitudinal Acceleration at 30 mph (d) Vertical Acceleration at 30 mph

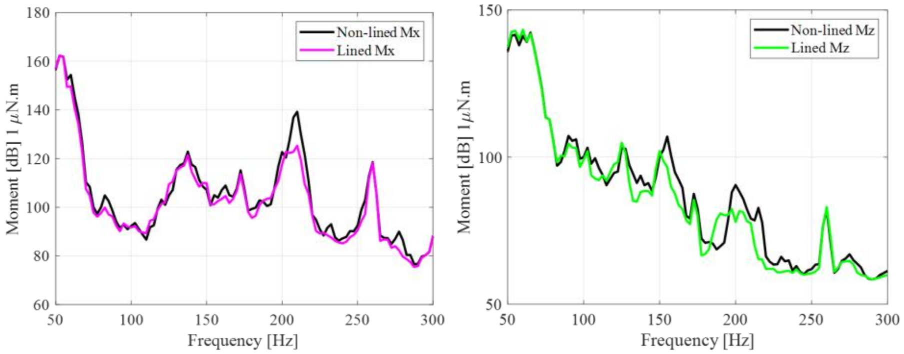

(e) Overturning moment around the fore aft axis expressed at 30 mph (f) Aligning moment about the vertical axis at 30 mph

Figure 4.12. Transmitted Acceleration, Force, and Moment of a Tire during Rolling at 30 mph.

In the sound pressure measurement though, the frequency reduction was well captured. As shown in Figure 4.13, the 1 inch and 2 inch porous linings significantly reduced the sound pressure level inside the tire and shifted the first cavity frequency from 207 Hz to 198 Hz and 182 Hz, respectively. These measurements confirm that our finite element analysis (FEA) model accurately predicts experimental results.

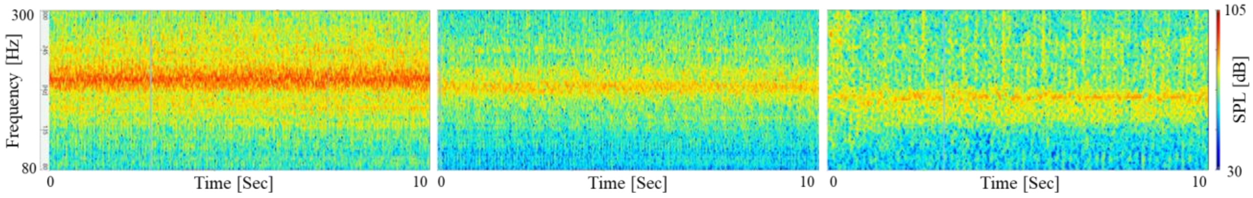

(a) non-lined, 210 Hz (b) 1” porous lined, 199 Hz (c) 2” porous lined, 184 Hz

Figure 4.13. Spectrogram of sound pressure inside of a rolling tire at 10 mph.

5. CONCLUSIONS AND FUTURE WORKS

5.1 Conclusions

In the present work, the frequency reduction and attenuation of the tire cavity resonance due to a porous lining has been investigated. The JCA model was adopted in the theoretical analysis to describe the sound propagation in the porous lining, thus allowing for a broader working boundary of design parameters and consideration of visco-inertial and thermal effects. The acoustic modeling was conducted based on a two-dimensional unfolded tire geometry and a transcendental equation was derived to compute the axial wavenumber in the tire. Integration of the JCA model and acoustic modeling predicted the frequency reduction and mode attenuation with respect to changes in design parameters. An important finding was the existence of not only the first optimal range previously identified by other researchers, but also a second optimal range that performed better in terms of attenuation. This new finding is further discussed next.

The investigation of the frequency reduction and mode attenuation of the tire cavity resonance was extended to a finite element analysis using a two-dimensional tire model with a porous lining. The simulation was conducted using the steady-state-dynamic mode of Abaqus software, and the first cavity frequency and sound pressure level were extracted and compared with the theoretical result. Interestingly, the second optimal range discovered in the theoretical analysis was also observed in the simulation. Furthermore, the case study demonstrated that a thin, but precisely engineered porous material with a second optimal FR could achieve comparable levels of attenuation to a thicker porous lining that was chosen without meticulous optimization. This finding has important implications for both porous material and tire manufacturers as it allows them to maximize performance while addressing issues such as cost, weight, and space limitations. As another output of the simulation, dispersion diagrams were generated by plotting the spatial Fourier transformed sound pressure inside the tire model. The diagrams revealed that the frequency reduction was a result of the slowed phase speed, and the mode attenuation was caused by the complex wavenumber due to the presence of the porous lining. The diagrams also indicate that the wave propagation within the lined tire was dispersive, with different frequency components traveling at different speeds while the wave type of the non-lined tire is non-dispersive.

In the experimental analysis, a porous material sample, an acoustic polyurethane foam, was selected and studied in the initial step. To estimate the design parameters, acoustic impedance was measured, and curve-fitting optimization was conducted. The resulting estimated design parameters fell approximately within the first optimal range. Measurements of the acceleration and force at the wheel center and the sound pressure inside a tire were taken and compared for both non-lined and lined tire cases. The results showed that the results from the finite element analysis aligned well with those from the experiments.

5.2 Future works

To further support the conclusions of this article, it is recommended that future research be conducted to create a sample in the second optimal region and have its performance validated. Additionally, the manufacturability and mass production feasibility of the sample should be investigated. The benefits and drawbacks of the second optimal sample should also be studied to ascertain if it can be considered as an effective countermeasure for tire air cavity resonance in the automotive market. Further, the use of a poro-elastic model of the foam would make it possible to predict the structural damping of tire vibration in addition to the sound attenuation.

APPENDIX. TIRE FORCE AND MOMENTS

1. Tractive (Longitudinal) force, F_X : The force of the road on the tire along the X-axis. The longitudinal force causes the acceleration/deceleration of the vehicle, depending on whether the tire is driven or braked. Positive longitudinal force (driving/driven force) is an indication that the tire is driven. Negative longitudinal force (braking force), is an indication that the tire is stopped.

2. Lateral force, F_Y: The force of the road on the tire along the Y-axis. Lateral force will cause a vehicle to move to the left or right depending on whether the tire is steered/cambered to either side.

3. Normal force, F_Z: The force of the road on the tire along the Z-axis. It is the contact force between the road and tire and will be on the contact patch. Normal force is always negative due to the direction of the force.

4. Overturning moment, M_X: The moment about the X-axis. Overturning moment is the effect of left-to-right displacement of the point of action of the normal force with respect to the contact center. Overturning moment will affect camber behavior and will often be used for finalizing camber adjustments, especially on race cars.

5. Rolling resistance moment, M_Y: The moment about the Y-axis. Rolling resistance moment represents the fore-aft displacement of the point of action of normal force with respect to the contact center.

6. Aligning moment, M_Z: The moment about the Z-axis. It represents the point of action of the shear forces (longitudinal and lateral force) within the road plane.

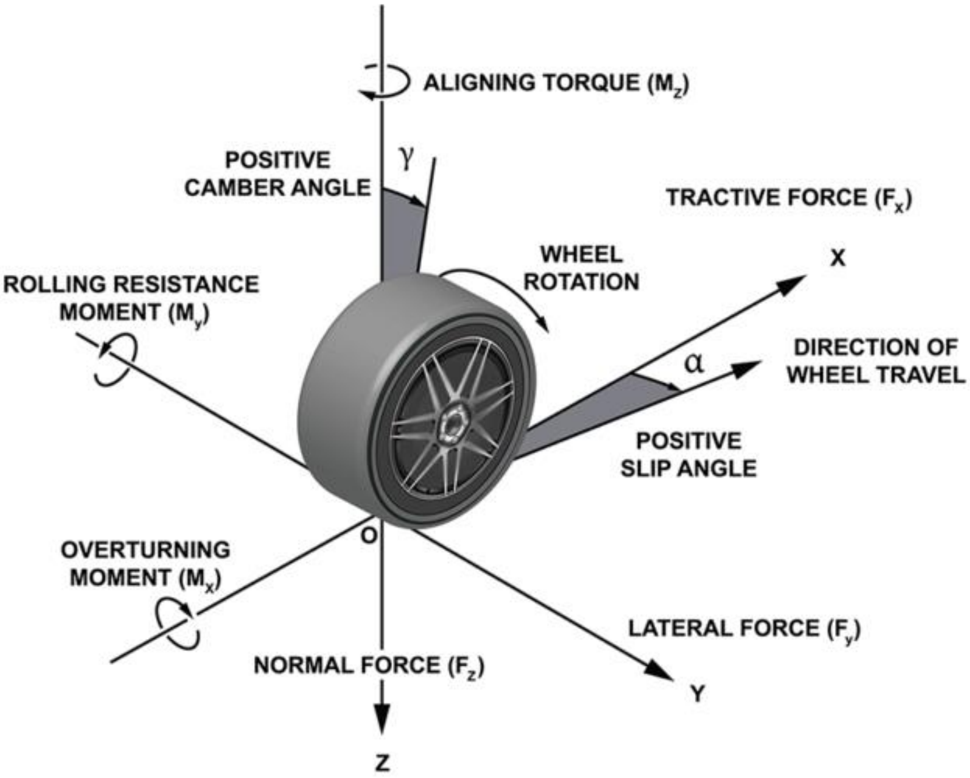

Figure A.1. Tire force and moments.

REFERENCES

[1] Duncan, A., Goetchius, G., and Guan, J. (2019). SAE 2019 NVH Conference Structure Borne NVH Workshop. SAE International.

[2] Michelin North America. (2020). An introduction to tire cavity noise. Michelin Acoustic Technology. https://www.michelinman.com/acoustic-technology.html

[3] Societe de Technologie Michelin. (2002). The tyre mechanical and acoustic comfort.

[4] Sakata, T., Morimura, H., and Ide, H. (1990). Effects of tire cavity resonance on vehicle road noise. Tire Science and Technology, 18(2), 68-79.

[5] Thompson, J. K. (1995). Plane wave resonance in the air cavity as a vehicle interior noise source. Tire Science and Technology, 23(1), 2-10.

[6] Sugiyama, H., Tanaka, Y., and Murata, S. (2020). Theoretical analysis for tire cavity resonance inside deformed stationary tire. Advanced Experimental Mechanics, 5, 163-168.

[7] Feng, Z. C., Gu, P., Chen, Y., and Li, Z. (2009). Modeling and experimental investigation of tire cavity noise generation mechanisms for a rolling tire. SAE International.

[8] Feng, Z. C., and Gu, P. (2011). Modeling and experimental verification of vibration and noise caused by the cavity modes of a rolling tire under static loading. SAE Technical Paper.

[9] Gonzalez Diaz, C., Kindt, P., Middelberg, J., Vercammen, S., Thiry, C., Close, R., and Leyssens, J., (2016). Dynamic behaviour of a rolling tyre: Experimental and numerical analyses. Journal of Sound and Vibration, 364, 147-164. https://doi.org/10.1016/j.jsv.2015.11.002

[10] Choi, W. H., and Bolton, J. S. (2021). Simulation of the frequency split of the fundamental air cavity mode of a loaded and rolling tire by using steady-state transport analysis. In INTER-NOISE 2021

[11] Liu, X., Zhao, W., Hu, X., Shan, Y., and He, T. (2022). Research on the resonance frequency splitting mechanism and novel modal characteristics of a rotating tire acoustic cavity. Journal of Vibration and Control, 0(0), 1-12. https://doi.org/10.1177/10775463211062561

[12] Cao, R., Sakamoto, N., & Bolton, J. S. (2014). Improved model for coupled structural-acoustics modes of tires. In Proceedings of the 2014 Noise Control Engineering Conference (pp. 1-10). Institute of Noise Control Engineering.

[13] Cao, R., and Bolton, J. S. (2015). Point excitation of a coupled structural-acoustical tire model with experimental verification. In INTER-NOISE 2015

[14] Baro, S., Corradi, R., and Åbom, M. (2016). Tyre cavity noise: Porous materials as a countermeasure. In INTER-NOISE 2016

[15] Baro, S., Corradi, R., Åbom, M., Caracino, P., and Fioravanti, A. P. (2019). Modelling of a lined tyre for predicting cavity noise mitigation. Applied Acoustics, 155, 391-400. https://doi.org/10.1016/j.apacoust.2019.05.029

[16] Zhang, Y., Yao, Q., Xiao, L., Zhang, X., Zheng, C., and Bi, C. (2019). On the resonance of a lined tire cavity. Acta Acustica united with Acustica, 105, 1237-1242. https://doi.org/10.3813/AAA.919357

[17] Wan, C., Zheng, C.-J., Bi, C.-X., and Zhang, Y.-B. (2022). Engineering analysis with boundary elements. Engineering Analysis with Boundary Elements, 143, 418-427. https://doi.org/10.1016/j.enganabound.2021.09.019

[18] Delany, M. E., and Bazley, E. N. (1970). Acoustical properties of fibrous absorbent materials. Applied Acoustics, 3, 105-116. https://doi.org/10.1016/0003-682X(70)90031-9

[19] Miki, Y. (1990). Acoustical properties of porous materials - Modifications of Delany-Bazley models. Journal of the Acoustical Society of Japan (E), 11(1), 19-24.

[20] Johnson, D. L., Koplik, J., and Dashen, R. (1987). Theory of dynamic permeability and tortuosity in fluid-saturated porous media. Journal of Fluid Mechanics, 176, 379-402. https://doi.org/10.1017/S0022112087000961

[21] Champoux, Y., and Allard, J.-F. (1991). Dynamic tortuosity and bulk modulus in air-saturated porous media. Journal of Applied Physics, 70, 1975-1979. https://doi.org/10.1063/1.349453

[22] Bolton, J. S. (2005). Porous Materials for Sound Absorption and Transmission Control. In Proceedings of Inter-Noise 2005. http://docs.lib.purdue.edu/herrick

[23] Gaulon, C., Pierre, J., Derec, C., Jaouen, L., Becot, F.-X., Chevillotte, F., Elias, F., Drenckhan, W., and Leroy, V. (2018). Acoustic absorption of solid foams with thin membranes. Applied Physics Letters, 112, 261904. https://doi.org/10.1063/1.5032159

[24] Jaouen, L. (n.d.). Viscous characteristic length. Matelys Research Lab. Retrieved March 18, 2023, from https://apmr.matelys.com/Parameters/ViscousCharacteristicLength.html

[25] Allard, J. F., and Atalla, N. (2009). Propagation of Sound in Porous Media: Modelling Sound Absorbing Materials (2nd ed.). John Wiley & Sons, Ltd.

[26] Seyyedi, S. M., Dogonchi, A. S., Hashemi-Tilehnoee, M., and Ganji, D. D. (2018). Improved velocity and temperature profiles for integral solution in the laminar boundary layer flow on a semi-infinite flat plate. Heat Transfer - Asian Research, 47(5), 1595-1604. https://doi.org/10.1002/htj.21378

[27] Dazel, O., Bécot, F.-X., & Jaouen, L. (2012). Biot effects for sound absorbing double porosity materials. Acta Acustica united with Acustica, 98(4), 567-576. https://doi.org/10.3813/AAA.918503

[28] Bécot, F.-X., & Jaouen, L. (2013). An alternative Biot's formulation for dissipative porous media with skeleton deformation. The Journal of the Acoustical Society of America, 134(6), 4801-4807. https://doi.org/10.1121/1.4829444

[29] Scott, R. A. (1946). The propagation of sound between walls of porous material. Proceedings of the Physical Society, 58, 358-366. https://doi.org/10.1088/0959-5309/58/3/307

[30] Kim, Y.-J., & Bolton, J. (2004). Effects of rotation on the dynamics of a circular cylindrical shell with application to tire vibration. Journal of Sound and Vibration, 275(3-5), 605-621. https://doi.org/10.1016/j.jsv.2003.07.008

[31] ASTM. (2012). Standard test method for impedance and absorption of acoustical materials using a tube, two microphones and a digital frequency analysis system (ASTM E1050-12). ASTM International. https://doi.org/10.1520/E1050-12

[32] Choi, W. H., Bolton, J. S., Haakenson, D., and Black, M. (2019). A Laboratory Procedure for Measuring the Dispersion Characteristics of Loaded Tires. In INTER-NOISE and NOISE-CON Congress and Conference Proceedings, NoiseCon19, San Diego, CA, pages 1-912 (pp. 851-860).

[33] Niknam, F. (2020, November 23). The Science Behind Ride & Handling, Tire Force and Moments (Courtesy of Yokohama Tire). Tire Review. https://www.tirereview.com/science-behind-ride-handling-tire-technology/